Development of a Hybrid En3DVar Data Assimilation System and Comparisons with 3DVar and EnKF for Radar Data Assimilation with Observing System Simulation Experiments

RONG KONG AND MING XUE

School of Meteorology, and Center for Analysis and Prediction of Storms, University of Oklahoma, Norman, Oklahoma

CHENGSI LIU

Center for Analysis and Prediction of Storms, University of Oklahoma, Norman, Oklahoma

(Manuscript received 8 June 2017, in final form 14 November 2017)

ABSTRACT

A hybrid ensemble–3DVar (En3DVar) system is developed and compared with 3DVar, EnKF, ''deterministic forecast'' EnKF (DfEnKF), and pure En3DVar for assimilating radar data through perfect-model observing system simulation experiments (OSSEs). DfEnKF uses a deterministic forecast as the background and is therefore parallel to pure En3DVar. Different results are found between DfEnKF and pure En3DVar: 1) the serial versus global nature and 2) the variational minimization versus direct filter updating nature of the two algorithms are identified as the main causes for the differences. For 3DVar (EnKF/DfEnKF and En3DVar), optimal decorrelation scales (localization radii) for static (ensemble) background error covariances are obtained and used in hybrid En3DVar. The sensitivity of hybrid En3DVar to covariance weights and ensemble size is examined. On average, when ensemble size is 20 or larger, a 5%–10% static covariance gives the best results, while for smaller ensembles, more static covariance is beneficial. Using an ensemble size of 40, EnKF and DfEnKF perform similarly, and both are better than pure and hybrid En3DVar overall. Using 5% static error covariance, hybrid En3DVar outperforms pure En3DVar for most state variables but underperforms for hydrometeor variables, and the improvement (degradation) is most notable for water vapor mixing ratio q_v (snow mixing ratio q_s). Overall, EnKF/DfEnKF performs the best, 3DVar performs the worst, and static covariance only helps slightly via hybrid En3DVar.

1. Introduction

To improve the accuracy of numerical weather prediction (NWP) at the convective scale, active research has been carried out in the past two decades to assimilate radar observations into numerical models. The assimilation of radar data using the traditional three-dimensional variational data assimilation (3DVar) approach or ensemble Kalman filtering (EnKF) has been shown to improve the prediction of convective systems (Hu et al. 2006a, b; Kain et al. 2010; Snook et al. 2011; Sun et al. 2014). More recently, the hybrid data assimilation (DA) approach that combines 3DVar and EnKF methods has been found to have some advantages over pure EnKF or pure 3DVar for large-scale DA (e.g., Buehner et al. 2010a, b, 2013; Clayton et al. 2013) and mesoscale DA (Li et al. 2012; Zhang et al. 2013; Pan et al. 2014).

3DVar is attractive for radar DA because of its relatively low computational cost and the ability to include weak equation constraints (Gao et al. 1999) to the cost function (Gao et al. 2004; Xiao et al. 2005; Hu et al. 2006b). However, the observation operator of radar reflectivity (Z) data is complicated; it involves multiple hydrometeor species and is highly nonlinear. Without additional physical constraints, the problem of assimilating reflectivity data within a 3DVar framework is underdetermined and/or nonunique. For this reason, indirect assimilation of Z is most commonly employed so far when using the 3DVar method, such as the use of a complex cloud analysis scheme (Hu et al. 2006a).

EnKF is an alternative method that has enjoyed increasing popularity in convective-scale DA, since its first application to radar DA by Snyder and Zhang (2003). In EnKF, flow-dependent background error covariances are derived from an ensemble of forecasts and used to update the state variables. EnKF allows for direct use of

Corresponding author: Ming Xue, mxue@ou.edu

DOI: 10.1175/MWR-D-17-0164.1

© 2018 American Meteorological Society. For information regarding reuse of this content and general copyright information, consult the AMS Copyright Policy (www.ametsoc.org/PUBSReuseLicenses).

nonlinear observation operators and is more suitable for a NWP model with complex parameterizations. The benefits of EnKF for convective-scale NWP and radar DA had been demonstrated in many studies (Tong and Xue 2005; Xue and Martin 2006; Xue et al. 2006; Jung et al. 2008; Tong and Xue 2008; Aksoy et al. 2009, 2010; Dowell et al. 2011; Snook et al. 2011; Stensrud et al. 2013; Snook et al. 2015). Zhang et al. (2011) and Stensrud et al. (2013) review some of the progress in recent years.

Although flow-dependent background error covariances can be approximated from ensemble forecasts in EnKF, the estimated covariance matrix is usually rank deficient because of the much smaller ensemble size compared to the degrees of freedom of NWP models (Houtekamer and Mitchell 1998; Hamill et al. 2000). Using much larger ensembles can help alleviate the problem but the computational cost can become prohibitively high. Covariance localization is commonly used to alleviate the rank-deficient problem (Hamill et al. 2001), but it has its own issues, such as preventing the use of distant correlations that are physically meaningful, or introducing imbalance into the background error cross correlations (Lorenc 2003; Houtekamer and Mitchell 2005; Kepert 2009; Greybush et al. 2011).

An alternative approach that can help alleviate the rank-deficiency problem is the so-called hybrid method; in which a weighted average of ensemble-derived flow-dependent background error covariance and the typical static flow-independent variational background error covariance is used. This strategy was first proposed by Hamill and Snyder (2000) while Lorenc (2003) proposed a computationally efficient implementation through introducing a set of extended control variables preconditioned on the ensemble covariance.

The advantages of the hybrid algorithms over traditional EnKF and 3DVar were first demonstrated using simulated observations and for the simple models (Hamill and Snyder 2000; Etherton and Bishop 2004; Wang et al. 2007), and the hybrid algorithm generally has more benefit when the ensemble size is small. The applications of hybrid algorithms to real cases are mostly at the large scales (Buehner et al. 2010a, b, 2013; Clayton et al. 2013) and mesoscales (Li et al. 2012; Zhang et al. 2013; Pan et al. 2014). For convective-scale radar DA, the development and testing of hybrid ensemble–variational (EnVar) algorithm have been more limited. Gao et al. (2013) first reported preliminary results comparing hybrid En3DVar, 3DVar, and EnKF for assimilating simulated radar data for a supercell storm. EnKF was found to outperform hybrid En3DVar with equal weights assigned to the static and ensemble covariances for the analyzed dynamic variables but underperform hybrid En3DVar for hydrometeor variables when assimilating data from single radar. When assimilating data from two radars, the hybrid method produced the best analyses for most model variables. Gao et al. (2014) further examined the dependency of the relative performance of hybrid En3DVar for different ensemble sizes and covariance weights, and they found that smaller ensemble sizes would benefit from a higher weight for the static covariance, consistent with earlier findings with larger-scale applications. In Gao et al. (2016), similar to Li et al. (2012), an ensemble of the 3D variational DA approach was taken in which the En3DVar system is run multiple times to provide the ensemble perturbations rather than running a parallel EnKF system. The sensitivities of supercell analyses to the inclusion of a mass continuity constraint, microphysics errors, and reflectivity assimilation were examined, again in an observing system simulation experiment (OSSE) framework. The assimilation of reflectivity data was found to accelerate storm spinup and have a small positive impact on wind analyses.

While interesting results have been obtained with the above studies through developing and testing hybrid algorithms for radar DA, further improvements and investigations are still needed. For example, the EnKF system used in Gao et al. (2013, 2014) was an experimental version of EnKF DA, and the 3DVar used constant background error variances for all state variables and empirical spatial correlation scales. If the background error covariances are further optimized for 3DVar and EnKF is optimally tuned in terms of covariance localization and inflation, would the relative performance of the 3DVar, EnKF, and En3DVar change? Also, in principle, when En3DVar uses 100% ensemble-derived covariance, its analysis should be identical to that of EnKF under linearity and Gaussian error assumptions; will their analyses actually be very close? If not, what are the sources of differences? In what situations does the static covariance in the hybrid algorithm help, if at all, for convective storms?

In this study, the above questions will also be addressed in an OSSE framework, under the assumption of a perfect prediction model. In the OSSEs, the truth is known, enabling a quantitative assessment of different algorithms. Based on the OSSEs, any difference between EnKF and En3DVar algorithms can be more easily investigated, and the potential benefits of hybrid En3DVar over traditional 3DVar and EnKF can be better demonstrated, if they do exist. This is necessary before applying hybrid DA to the real cases where many possible, unknown sources of error make understanding the performance of the algorithms difficult. From a

broader perspective, it is also helpful for algorithm improvements in the future, and providing a better initial condition for operational numerical prediction of convective weather systems.

The hybrid En3DVar algorithm based on the extended control variable approach of Lorenc (2003) is implemented within the ARPS 3DVar framework (Gao et al. 2004). The En3DVar system is coupled with a mature EnKF DA system that has been developed and tested for radar data DA over the past decade to form a coupled EnKF–hybrid En3DVar system. To facilitate the most fair and direct comparison between EnKF and pure En3DVar, we formulate an alternative EnKF algorithm in which an additional deterministic forecast is produced each cycle which is updated in the same manner as the ensemble mean background in the EnKF, and we call this algorithm DfEnKF (because of the use of deterministic forecast), and DfEnKF will be directly compared with pure En3DVar. We aim to answer some of the questions posed in the earlier paragraph.

The rest of this paper is organized as follows. In section 2, we introduce various DA algorithms (EnKF, DfEnKF, and En3DVar) as well as the design of the OSSE experiments. In section 3, pure En3DVar is first compared with DfEnKF and the reasons for their differences are investigated. Sensitivity experiments are conducted to obtain the optimal localization radii, optimal background error decorrelation scales, and optimal hybrid weights for EnKF/pure En3DVar, 3DVar, and hybrid En3DVar algorithms, respectively. Finally, optimally configured hybrid En3DVar, 3DVar, and EnKF are intercompared. The summary and conclusions are presented in section 4, with some additional discussion.

2. Assimilation algorithms and experimental design

a. The EnKF system

The EnKF system used in this study was initially developed for the ARPS model, as originally described in Tong and Xue (2005), Xue et al. (2006), and Tong and Xue (2008). The ensemble square root filter (EnSRF) algorithm of Whitaker and Hamill (2002) is used, which updates the ensemble mean and ensemble perturbations without perturbing the observations. Following Whitaker and Hamill (2002) and Xue et al. (2006), the EnSRF analysis equations are briefly described in the following.

The ensemble mean forecast is first updated by Eq. (1) below:

$$\overline{\mathbf{x}}^a = \overline{\mathbf{x}}^b + \mathbf{K}[\mathbf{y} - \overline{H(\mathbf{x}^b)}], \tag{1}$$

where

$$\mathbf{K} = [\boldsymbol{\rho}_s \circ (\mathbf{P}^b\mathbf{H}^{\mathrm{T}})](\mathbf{H}\mathbf{P}^b\mathbf{H}^{\mathrm{T}} + \mathbf{R})^{-1}. \tag{2}$$

In the equations, $\overline{\mathbf{x}}^a$ and $\overline{\mathbf{x}}^b$ are the ensemble mean analysis and background forecast state vectors, respectively; $\mathbf{y}$ is the observation vector; H is the observation operator; $\mathbf{H}$ is the tangent linear observation operator; $\mathbf{K}$ is the Kalman gain; $\mathbf{P}^b$ is the background error covariance; $\mathbf{R}$ is the observation error covariance matrix; and $\mathbf{P}^b\mathbf{H}^{\mathrm{T}}$ and $\mathbf{H}\mathbf{P}^b\mathbf{H}^{\mathrm{T}}$ are the background error covariances defined between the grid points and observation points, and between the observation points, respectively, and are evaluated directly from the ensemble background states $\mathbf{x}_k^b$ (k is the index of ensemble member) and their observation counterparts, $H(\mathbf{x}_k^b)$, called observation priors. A distance-dependent localization function (Gaspari and Cohn 1999) is used for the localization of the ensemble covariance; $\boldsymbol{\rho}_s \circ$ denotes a Schur product of the correlation matrix $\boldsymbol{\rho}_s$.

The ensemble perturbations, denoted by superscript prime, are updated by

$$\mathbf{x}_k'^a = \mathbf{x}_k'^b - \tilde{\mathbf{K}}H(\mathbf{x}_k^b)' \tag{3}$$

and

$$H(\mathbf{x}_k^b)' = H(\mathbf{x}_k^b) - \overline{H(\mathbf{x}^b)}, \tag{4}$$

where $\tilde{\mathbf{K}}$ is the "reduced" Kalman gain that is equal to $\mathbf{K}$ amplified by a factor following Whitaker and Hamill (2002) and the actual formula can be found in Xue et al. (2006). The final analyses for the ensemble members are

$$\mathbf{x}_k^a = \overline{\mathbf{x}}^a + \mathbf{x}_k'^a. \tag{5}$$

For more detailed descriptions related to the calculation of ensemble mean and ensemble covariance, please refer to Xue et al. (2006).

b. The DfEnKF algorithm

For the convective scale, the ensemble forecast mean tends to smooth out detailed convective-scale structures that are important. Therefore, the mean of ensemble forecasts may not necessarily be the best representation of convective storms (Yussouf et al. 2013). In En3DVar cycles, the background forecast is a deterministic forecast starting from the En3DVar analysis of the previous cycle. To facilitate more direct comparison of the EnKF results with those of En3DVar, and to potentially improve the results of EnKF, we developed an alternative implementation of EnKF, in which a separate set of analysis and forecast is run that uses a deterministic forecast $\mathbf{x}_d^b$ in place of the ensemble mean background

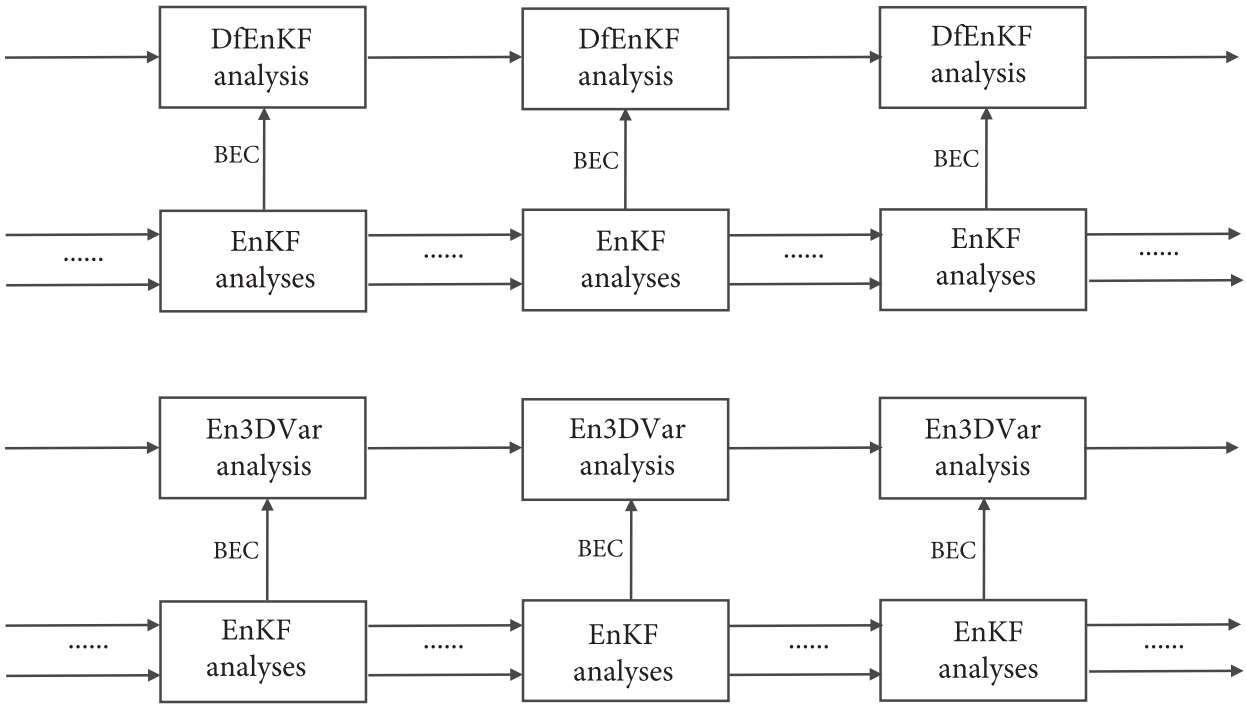

FIG. 1. Flowchart of the cycles in one-way coupling between EnKF and DfEnKF and EnKF and En3DVar analysis schemes, where BEC represents the background error covariance. The ensemble perturbations are updated by the EnKF.

forecast $\overline{\mathbf{x}}^b$ in the ensemble mean update in Eq. (1), to obtained analysis $\mathbf{x}_d^a$:

$$\mathbf{x}_d^a = \mathbf{x}_d^b + \mathbf{K}[\mathbf{y} - H(\mathbf{x}_d^b)]. \tag{6}$$

The deterministic forecast is started from this version of EnKF analysis, and we call this EnKF formulation DfEnKF, where Df denotes deterministic forecast.

Figure 1 shows the flow charts of the DfEnKF and En3DVar DA one-way coupled with EnKF. Similar to En3DVar, DfEnKF can be treated as an independent algorithm that borrows the ensemble covariance from the EnKF, and updates its single background field based on the EnKF mean update equation (the EnSRF algorithm is used here).

It is worth noting that our DfEnKF algorithm is different from the so-called deterministic EnKF (DEnKF) proposed by Sakov and Oke (2008), which modifies the original EnKF perturbation updating equations by using only half of the Kalman gain matrix and avoids perturbing the observations. Given that we use the EnSRF algorithm that does not perturb observations, our DfEnKF algorithm is also a deterministic EnKF algorithm.

We point out here that one may choose to replace the ensemble mean analysis of the regular EnKF with the analysis of DfEnKF so that the ensemble perturbations are effectively defined around the DfEnKF analysis; doing so results in a "two-way-coupled" DfEnKF and EnKF systems, as in a two-way-coupled En3DVar–EnKF system. In this paper, we choose one-way coupling to keep the algorithms more independent so that performances of different algorithms can be more clearly compared. If better analysis can be obtained from En3DVar and DfEnKF than EnKF, the overall performance can be improved by replacing the ensemble mean of EnKF with the En3DVar or DfEnKF analyses (i.e., allowing for the two-way interactions).

c. *The En3DVar system*

The hybrid En3DVar DA algorithm is implemented within the existing ARPS 3DVar variational framework (Gao et al. 2004). The hybrid En3DVar algorithm is based on the extended control variable method of Lorenc (2003) although the actual formulations follow Liu and Xue (2016) more closely. The combined use of the full-rank static background error covariance and the rank-deficient ensemble covariance in En3DVar is achieved through the extended state vector method. The analysis increment is given by

$$\Delta\mathbf{x}^a = \mathbf{x}^a - \mathbf{x}^b = \beta_1\Delta\mathbf{x}_1 + \beta_2\Delta\mathbf{x}_2, \tag{7}$$

$$\beta_1^2 + \beta_2^2 = 1, \tag{8}$$

where $\Delta\mathbf{x}_1$ and $\Delta\mathbf{x}_2$ are the analysis increments related to the static and ensemble background error covariances,

respectively; and β_1^2 and β_2^2 are the weights given to the static and ensemble covariances, respectively:

$$\Delta \mathbf{x}_1 = \mathbf{U}\mathbf{v}, \tag{9}$$

$$\mathbf{B} = \mathbf{U}\mathbf{U}^{\mathrm{T}}, \tag{10}$$

$$\Delta \mathbf{x}_2 = \sum_{i=1}^{N} (\mathbf{x}'_{bi} \circ \boldsymbol{\alpha}_i), \tag{11}$$

$$\boldsymbol{\alpha} = \begin{bmatrix} \boldsymbol{\alpha}_1 \\ \vdots \\ \boldsymbol{\alpha}_N \end{bmatrix}, \tag{12}$$

where $\mathbf{v}$ is the traditional variational control variable (vector) preconditioned on the square root of the 3DVar static background error covariance $\mathbf{B}$; $\mathbf{U}$ is the square root of $\mathbf{B}$; $\mathbf{x}'_b$ is a matrix of ensemble perturbations normalized by $\sqrt{N-1}$, which has N state vectors; $\mathbf{x}'_{bi} = \mathbf{x}_{bi} - \overline{\mathbf{x}}^b$ whose dimension is n; and N and n are the ensemble size and the dimension of state vector, respectively. The open circle symbol ($\circ$) denotes the Schur product:

$$\boldsymbol{\alpha} = \begin{bmatrix} \mathbf{C}' & & \\ & \ddots & \\ & & \mathbf{C}' \end{bmatrix} \tilde{\boldsymbol{\alpha}}. \tag{13}$$

Here $\tilde{\boldsymbol{\alpha}}$ is a new control vector related to the extended control vector $\boldsymbol{\alpha}$, an $n \times n$ correlation matrix $\mathbf{C}$ is used to localize the ensemble covariance, and $\mathbf{C}'$ is the corresponding decomposed matrix that satisfies $\mathbf{C} = \mathbf{C}'\mathbf{C}'^{\mathrm{T}}$. A hybrid solution is derived by setting β_1 or β_2 to values between but not equal to 0 and 1.

The analysis increment in Eq. (7) is obtained via minimizing the following cost function:

$$J(\mathbf{v}, \tilde{\boldsymbol{\alpha}}) = \frac{1}{2}\mathbf{v}^{\mathrm{T}}\mathbf{v} + \frac{1}{2}\tilde{\boldsymbol{\alpha}}^{\mathrm{T}}\tilde{\boldsymbol{\alpha}} + \frac{1}{2}\left[\beta_1 \mathbf{H}\mathbf{U}\mathbf{v} + \beta_2 \mathbf{H}\sum_{i=1}^{N}(\mathbf{x}'_{bi} \circ \mathbf{C}'\tilde{\boldsymbol{\alpha}}_i) + \mathbf{d}\right]^{\mathrm{T}} \times \mathbf{R}^{-1}\left[\beta_1 \mathbf{H}\mathbf{U}\mathbf{v} + \beta_2 \mathbf{H}\sum_{i=1}^{N}(\mathbf{x}'_{bi} \circ \mathbf{C}'\tilde{\boldsymbol{\alpha}}_i) + \mathbf{d}\right], \tag{14}$$

where $\mathbf{d}$ is the observation innovation vector. Additional details can be found in Liu and Xue (2016).

In this study, as is typically done, the En3DVar is coupled with EnKF to form a coupled EnKF–En3DVar system, where the EnKF system provides ensemble perturbations to En3DVar for flow-dependent covariance, while En3DVar itself updates a single background forecast to obtain a single new analysis. Figure 1 illustrates the one-way coupling between EnKF and En3DVar. With two-way coupling, the analysis of En3DVar is used to replace the ensemble mean analysis of EnKF [i.e., $\mathbf{x}^a$ from Eq. (7) is used to replace $\overline{\mathbf{x}}^a$ in Eq. (1)]. As mentioned earlier, in this paper, we choose to stick with one-way coupling to keep the algorithms more separate (so that they are not too mingled) for comparison purposes.[1] When the ensemble-derived covariance is used at 100% without static covariance, the En3DVar is referred to as pure En3DVar. When static and ensemble covariances are used in combination, the algorithm is referred to as hybrid En3DVar. Full ensemble covariance localization is implemented in all three directions via the correlation matrix in the extended control variable term in the cost function. The readers are referred to Liu and Xue (2016) for discussions on related terminology. The static background error covariances for the hydrometeors adopt temperature-dependent vertical profiles we recently proposed to improve variational analyses of hydrometeors from reflectivity observations.

d. *The prediction model and truth simulation for OSSEs*

In this study, the nonhydrostatic ARPS (Xue et al. 2000, 2001, 2003) is used as the prediction model for EnKF and En3DVar DA cycles. The En3DVar algorithm developed is compared with 3DVar and EnKF via perfect-model OSSEs. Simulated radial velocity and reflectivity data from a single Doppler radar are assimilated for a tornadic supercell storm. A sounding derived from that of the 20 May 1977 in Del City, Oklahoma (Ray et al. 1981), supercell storm case is used to define the storm environment. The Lin et al. (1983) ice microphysics parameterization is used.

The model configurations follow closely those of Tong and Xue (2005). Specifically, the model grid size is 35× 35 × 35; and the grid resolutions are 2 km and 0.5 km in the horizontal and vertical directions, respectively. The storm in the truth simulation is triggered by an elliptical thermal bubble with a 4-K maximum temperature perturbation, and the bubble is located at 24, 16, and 1.5 km in the x, y, and z directions. The horizontal and vertical radii of the bubble are 10 km and 1.5 km, respectively. A constant wind of (3, 14) m s^{-1} is subtracted from the original sounding so that the supercell could remain within the simulation domain. The storm is simulated up

[1] For the relatively short period of DA cycles presented in this paper, the two coupling systems generally will not diverge from each other much; for long periods of DA cycles, two-way coupling is recommended.

to 2 h with an evolution similar to those documented in Tong and Xue (2005). For EnKF, a distance-dependent localization function following Gaspari and Cohn (1999) is used to localize the ensemble covariance, while the covariance localization in En3DVar is realized through recursive filters applied to the extended control variable term of the cost function [corresponding to the second term on the right-hand side of Eq. (14)], to realize similar localization effects in the En3DVar algorithm. When the vertical model grid is stretched, the vertical localization realized through the recursive filter in the En3DVar algorithm is usually asymmetric; to avoid this complication when comparing the EnKF and En3DVar algorithms, we choose to utilize a vertically uniform grid, which is also used in the OSSEs of Tong and Xue (2005).

e. Simulation of the radar observations

The radial velocity v_r and reflectivity Z data are simulated based on the model velocity and mixing ratios of hydrometeor fields, respectively, with the following formula:

$$v_r = u \sin\phi \cos\mu + v \cos\phi \cos\mu + w \sin\mu, \quad (15)$$

$$Z_e = Z_{er}(q_r) + Z_{es}(q_s) + Z_{eh}(q_h), \quad (16)$$

$$Z = 10 \log_{10}^{Z_e}. \quad (17)$$

Here, ϕ and μ are the azimuth and elevation angles of radar beams; u, v, and w are the model velocity components in the observational space that are interpolated from the truth simulation grid; Z_e is the equivalent radar reflectivity factor, which contains contributions from the mixing ratios of rain q_r, snow q_s, and hail q_h, respectively; and Z (in dBZ) is the reflectivity factor and is the quantity assimilated. The actual reflectivity formula for the individual components follow those given in Tong and Xue (2005). The default values of the intercept parameters of the size distributions of the hydrometeors in the Lin et al. (1983) are used, as in Tong and Xue (2005). Equations (15)–(17) are also the observation operators for radial velocity and reflectivity data in the DA systems.

One WSR-88D is assumed to be located at the origin (i.e., the southwest corner) of the simulation domain, and its data are simulated based on the truth simulation. Unbiased and normal distributed random errors with standard deviations of 3 dBZ and 1 m s^{-1} are added to the simulated reflectivity and radial velocity data, respectively. The same error standard deviations are also specified in the DA. The simulated reflectivity and radial velocity observations are collected on 14 elevation levels ranging from 0.5° to 19.5° based on volume coverage pattern 11 (VCP11) in precipitation mode. The maximum radar coverage is 230 km. Radial velocity data are assimilated only in regions where truth reflectivity is greater than 15 dBZ in the analysis domain, while reflectivity data in precipitation regions (values ≥5 dBZ) only are assimilated.

f. Design of assimilation experiments

The simulated storm cell is well developed after 25 min of model integration. Same as Tong and Xue (2005), the unbiased and Gaussian-distributed random perturbations are added to the sounding-defined first-guess field to generate the initial ensemble perturbations. The standard deviations are 2 K for potential temperature θ; 2 m s^{-1} for velocity components u, v, and w; and 0.6 g kg^{-1} for mixing ratios of water vapor and hydrometeor fields, respectively. Previous studies have shown that adding random perturbations to the whole domain would introduce a lot of noise into the model fields (Snyder and Zhang 2003; Dowell et al. 2004). Different from Tong and Xue (2005), the perturbations of u, v, w, and θ are confined to the regions with observed reflectivity higher than 0 dBZ, and hydrometeor perturbations are confined to regions with reflectivity higher than 15 dBZ. The radial velocity and reflectivity observations are assimilated every 5 min for one hour, with the first assimilation performed at 30 min of the truth simulation time. Experiments with different combinations of localization radii and recursive filter length scales in horizontal and vertical directions are first tested to obtain the optimal localization radii and recursive filter length scales for EnKF and En3DVar, respectively.

To obtain more physical hydrometeor analyses, height-dependent (or in a more general form temperature dependent) static background error profiles for different hydrometeors are used in 3DVar, and in hybrid En3DVar (for the static background error). Specifically, the background error of snow at the low levels (<4 km) is set to values two orders of magnitude smaller than the error at other levels (set to 0.6 g kg^{-1}), which ensures small analysis increments of snow at the lower levels (below freezing levels). The background error of rainwater at higher levels (>8 km) are set to values one order of magnitude smaller than default value of 0.6 g kg^{-1} to help prevent unphysical rainwater analysis increments at the upper levels. For levels between 4 and 8 km, 1/5 of the default value (i.e., 0.1 g kg^{-1}) is used in this study to suppress analysis increment of rainwater but still allow for the existence of supercool water close to and higher than the freezing level. The background error of hail is 0.6 g kg^{-1} at all levels; considering that hail can fall below the freezing level (Liu et al. 2016). This strategy of using height or temperature-dependent hydrometeor background error profiles within 3DVar is a subject of a separate paper, and is therefore only briefly described here.

TABLE 1. Descriptions of the assimilation methods.

Method	Use of background error covariance	Background updating	Ensemble size
3DVar	Static background error covariance	Update background field deterministically	—
EnKF	Background error covariance derived from ensemble background forecasts	Updates ensemble mean background and ensemble perturbations using EnKF algorithm	40
DfEnKF	Using ensemble covariance from an EnKF system	Update a single deterministic background forecast using EnKF mean updating algorithm	40
Pure En3DVar	Using 100% ensemble covariance from an EnKF system	Update a single deterministic background forecast using variational algorithm	40
Hybrid En3DVar	Using weighted average of ensemble covariance and static 3DVar covariance	Update a single deterministic background forecast using variational algorithm	10, 20, . . . , 100

We perform five types of experiments that are named same as the methods they use (Table 1). The first three types are 3DVar, EnKF, and DfEnKF that use the standalone static background error covariance $\mathbf{B}$ and ensemble covariance $\mathbf{P}^b$, respectively. The remaining two types are the pure En3Dvar that uses 100% ensemble covariance and the hybrid En3DVar that uses a combination of the static and ensemble covariance, respectively. Performances of DfEnKF and pure En3DVar are compared, and the reasons for differences are investigated though sensitivity experiments. Hybrid En3DVar with different combinations of ensemble members and ensemble covariance weights are tested to see the sensitivity of the hybrid analysis to these factors. Finally, Hybrid En3DVar is compared with 3DVar, EnKF, and pure En3DVar to see if hybrid En3DVar has any advantage over other methods.

3. Results of assimilation experiments

To evaluate the performance of algorithms in different experiments, we define a mean error that is the average of the RMSEs of both the analysis and 5-min background forecast at all analysis times scaled by the background RMSE at the beginning of the assimilation window (at 25 min). The actual error formulation is

$$\overline{\varepsilon} = \frac{1}{2(N+1)\varepsilon_0}\sum_{t=0}^{N}(\varepsilon_{bt} + \varepsilon_{at}), \tag{18}$$

where $\overline{\varepsilon}$ is the mean error; ε_{bt} and ε_{at} are the gridpoint average of the RMSEs at time t for a certain variable from the background and the analysis fields, respectively; ε_0 is the gridpoint average of the RMSEs at the beginning of the assimilation window, which are the same for all experiments; and N is the total number of assimilation cycles. The RMSEs are calculated only over grid points where the truth reflectivity is higher than 15 dBZ. We refer to the mean error defined in Eq. (18) as the mean scaled RMSE for a specific variable. An additional average can be calculated over all variables to give an overall mean RMSE.

a. *Comparison of DfEnKF and pure En3DVar results*

1) OPTIMAL LOCALIZATION RADII FOR DFENKF AND ENKF

In EnKF, a Gaussian-like fifth-order piecewise polynomial of Gaspari and Cohn (1999) is used for covariance localization. Sensitivity experiments with different combinations of the horizontal and vertical cutoff radii of localization that range from 1 km to 20 (15) km in horizontal (vertical) with a 1-km interval are conducted for DfEnKF. As indicated in Fig. 2, the optimal localization radii for different variables are similar except for hail mixing ratio, and on average the combination of 15 and 6 km for horizontal and vertical cutoff radii yields the best result in terms of the minimal analysis and forecast errors. Similarly, Sobash and Stensrud (2013) found that ~12–18-km horizontal and ~3-km vertical localization cutoff radii were beneficial for their EnKF experiments with 50 ensemble members and a 3-km grid resolution. On the "optimal" localization radii, some discrepancies between this and previous studies are worth mentioning. For example, Tong and Xue (2005) noted that a localization radius of 6 km produced the best result with 100 ensemble members, but their optimal radii were obtained based on the assumption that the horizontal and vertical localization radii were the same.

Sensitivity experiments show that the optimal localization radii for EnKF are almost the same as those for DfEnKF, so the optimal localization radii of DfEnKF are adopted as the common optimal localization radii for both EnKF and DfEnKF in later experiments.

Unlike DfEnKF that uses a fifth-order Gaussian-like polynomial function and a Schur product [see Eq.(2)] to localize the ensemble covariance, En3DVar uses a recursive filter in each coordinate direction to mimic a

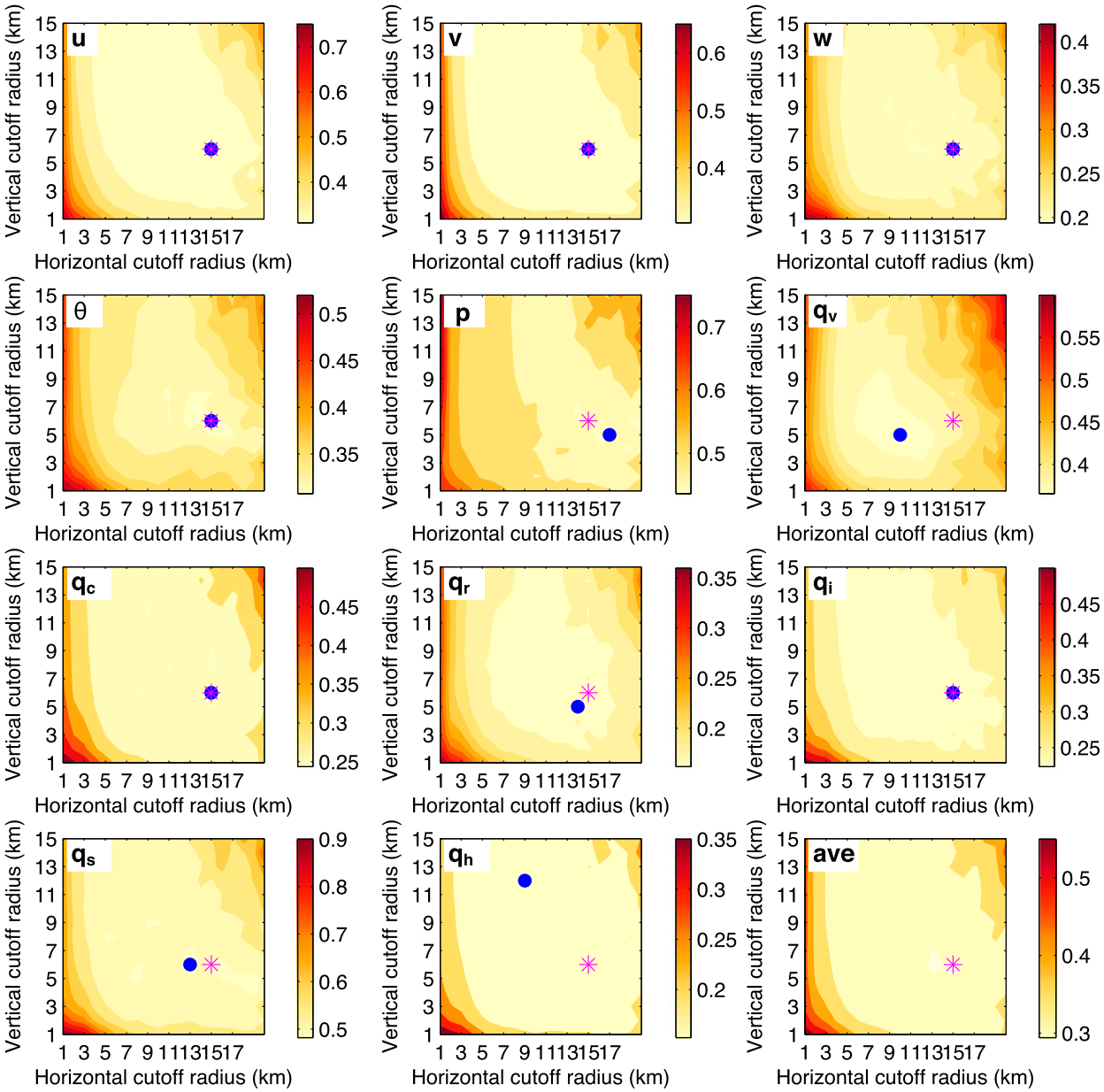

FIG. 2. The scaled RMSEs for different state variables as defined in Eq. (18) and averaged over all variables (ave), for DfEnKF experiments with different combinations of horizontal and vertical cutoff radius (km). The blue dot in each panel indicates the location of minimum scaled RMSE for the corresponding variable and the magenta asterisk indicates the minimum value across all the variables.

second-order autoregressive function (that is close to Gaussian) for the localization. To investigate the source of difference between pure En3DVar and DfEnKF, the optimal localization radii of DfEnKF are also used by pure En3DVar in this section. The recursive filter length scale S_{RF} and the cutoff radius of DfEnKF localization S_{GC} can be roughly converted from each other based on the following equation:

$$S_{RF} = \sqrt{0.15} S_{GC} / \sqrt{2}, \tag{19}$$

which is given as Eq. (4) in Pan et al. (2014). The equivalent recursive-filter length scales for localization in En3DVar are therefore 4.11 km in the horizontal and 1.64 km in the vertical, corresponding to the 15- and 6-km cutoff localization radii, respectively. In next section, the optimal localization radii of En3DVar will be determined by similar sensitivity experiments and En3DVar will be compared with other algorithms with their own optimal localization radii.

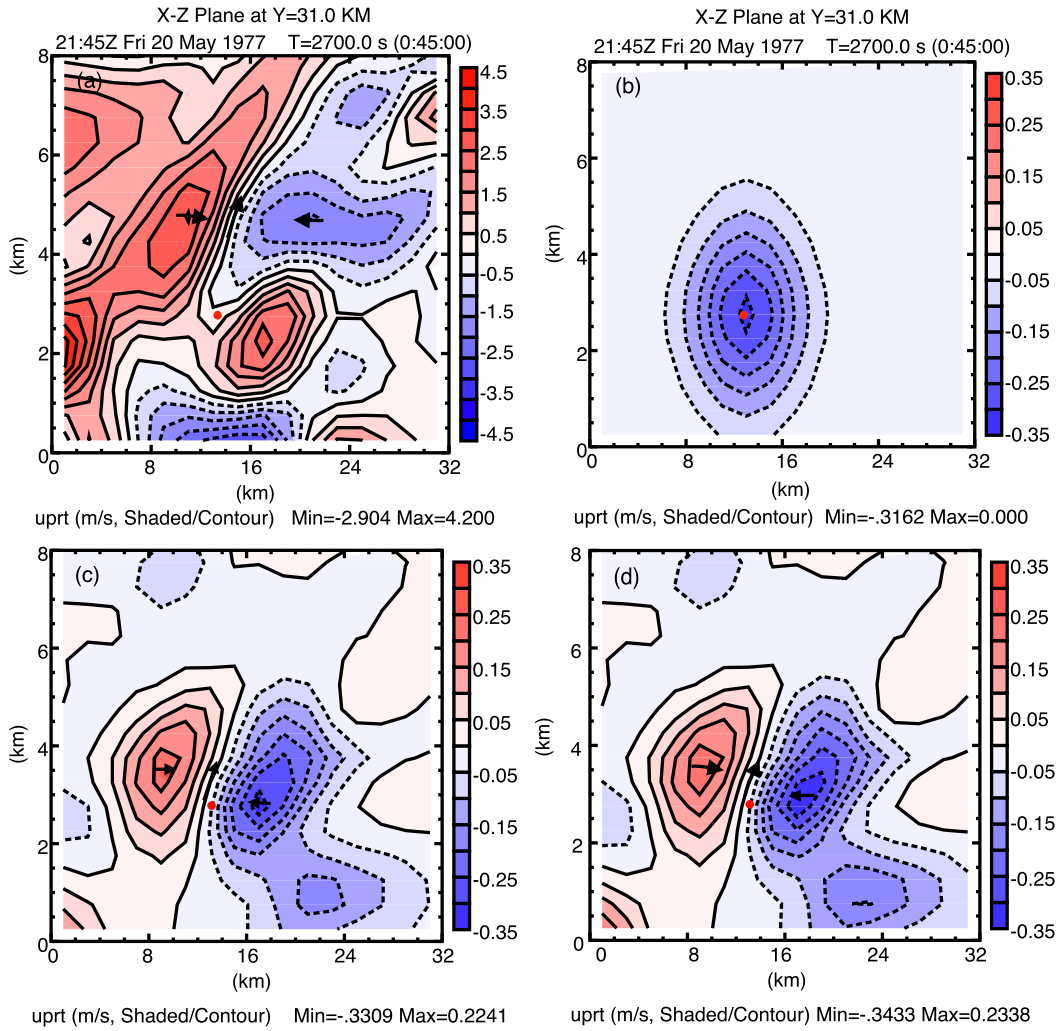

FIG. 3. Vertical cross sections of (a) the truth minus background, and the analysis increment (analysis minus background) of u wind ($\mathrm{m\,s^{-1}}$) when assimilating radial velocity at a single point, using (b) 3DVar, (c) pure En3DVar, and (d) DfEnKF, respectively. Horizontal convergence and upward motion are indicated by the horizontal and vertical black arrows, respectively.

2) SINGLE-OBSERVATION EXPERIMENTS WITH DFENKF, PURE EN3DVAR, AND 3DVAR

Single-observation experiments are often used to examine the correctness of newly developed DA systems, and the effects of spatial spreading of observation innovation by the background error covariance (Hu et al. 2006b; Zhu et al. 2013). The flow-dependent nature of the ensemble covariance in pure En3DVar and DfEnKF can be revealed by single-observation experiments. In our experiments, a single radial velocity observation is taken at a model grid point near the updraft region (as indicated by the upward vector in Fig. 3). The single-observation test uses background ensemble forecasts from the fourth cycle of a cycled EnKF experiment. En3DVar uses the localization radii that are equivalent to the optimal localization configurations of DfEnKF.

For the single radial velocity DA experiment, the analysis increment of u wind is positive (negative) to the left (right) of the updraft for both pure En3DVar and DfEnKF (Figs. 3c and 3d), which is more consistent with the true increment (which is the truth minus background) in Fig. 3a, while for 3DVar, the analysis increment is a flow-independent ellipse that is not realistic (Fig. 3b). Similarly, for single reflectivity observation assimilation, the analysis increments of the hail mixing ratio for En3DVar and DfEnkF are similar and show flow-dependent structures while that of 3DVar is again elliptical (Fig. 4). An important point to note is that 3DVar creates the hail mixing ratio increment symmetrically above and below the

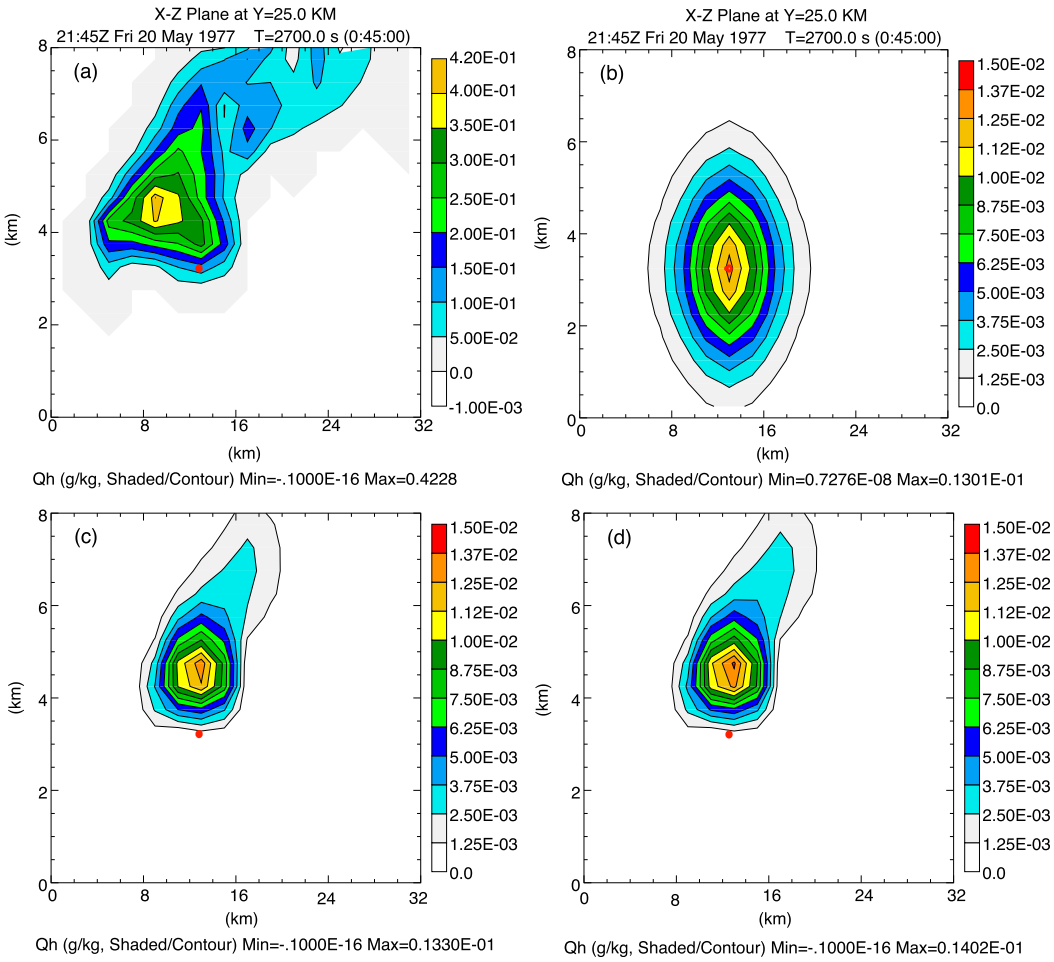

FIG. 4. Vertical cross sections of (a) truth minus background, and analysis increment (analysis minus background) for hail mixing ratio ($\mathrm{g\,kg^{-1}}$) when assimilating a single reflectivity observation at the red dot location, using (b) 3DVar, (c) En3DVar, and (d) DfEnKF, respectively.

observation point, with the increment extending way below the freezing level, which in this case is unrealistic. In En3DVar and DfEnKF, the flow-dependent covariance is aware of the temperature dependency of hail distributions.

Another point worth mentioning is that radial velocity assimilation only updates the wind fields (u, v, w) and reflectivity assimilation only updates hydrometeors (q_r, q_s, q_h) in 3DVar. In EnKF and En3DVar, however, all model prognostic variables can be updated via background error cross correlations; this is an important advantage for algorithms utilizing the ensemble-derived background error covariances.

3) OSSE COMPARISONS BETWEEN DFENKF AND PURE EN3DVAR

In this section, the performances of EnKF, DfEnKF, and pure En3DVar are compared by assimilating both radial velocity and reflectivity data every 5 min for 1 h. When using the optimal localization radii of DfEnKF, DfEnKF clearly outperforms pure En3DVar in terms of smaller RMSEs, especially for snow and some of the other hydrometeor variables (Fig. 5). Only pressure p has larger errors in some of the earlier cycles when using DfEnKF (Fig. 5), but pressure is more sensitive to acoustic noises, as pointed out by Tong and Xue (2005).

To see how well the precipitation fields are analyzed, the reflectivity components from individual hydrometeor mixing ratios are calculated according to

$$Z_x = 10\log_{10}(Z_{ex}), \tag{20}$$

where Z_{ex} is the equivalent reflectivity; x represents r, s, *or* h for rain, snow, and hail, respectively; Z_x is the corresponding reflectivity in dBZ and is introduced here for convenience only; and the total reflectivity $Z = 10\log_{10}(Z_{er} + Z_{es} + Z_{eh})$, is not equal to the sum of Z_r, Z_s, and Z_h. Horizontal cross sections of the analyzed reflectivity and contributions to reflectivity from snow and

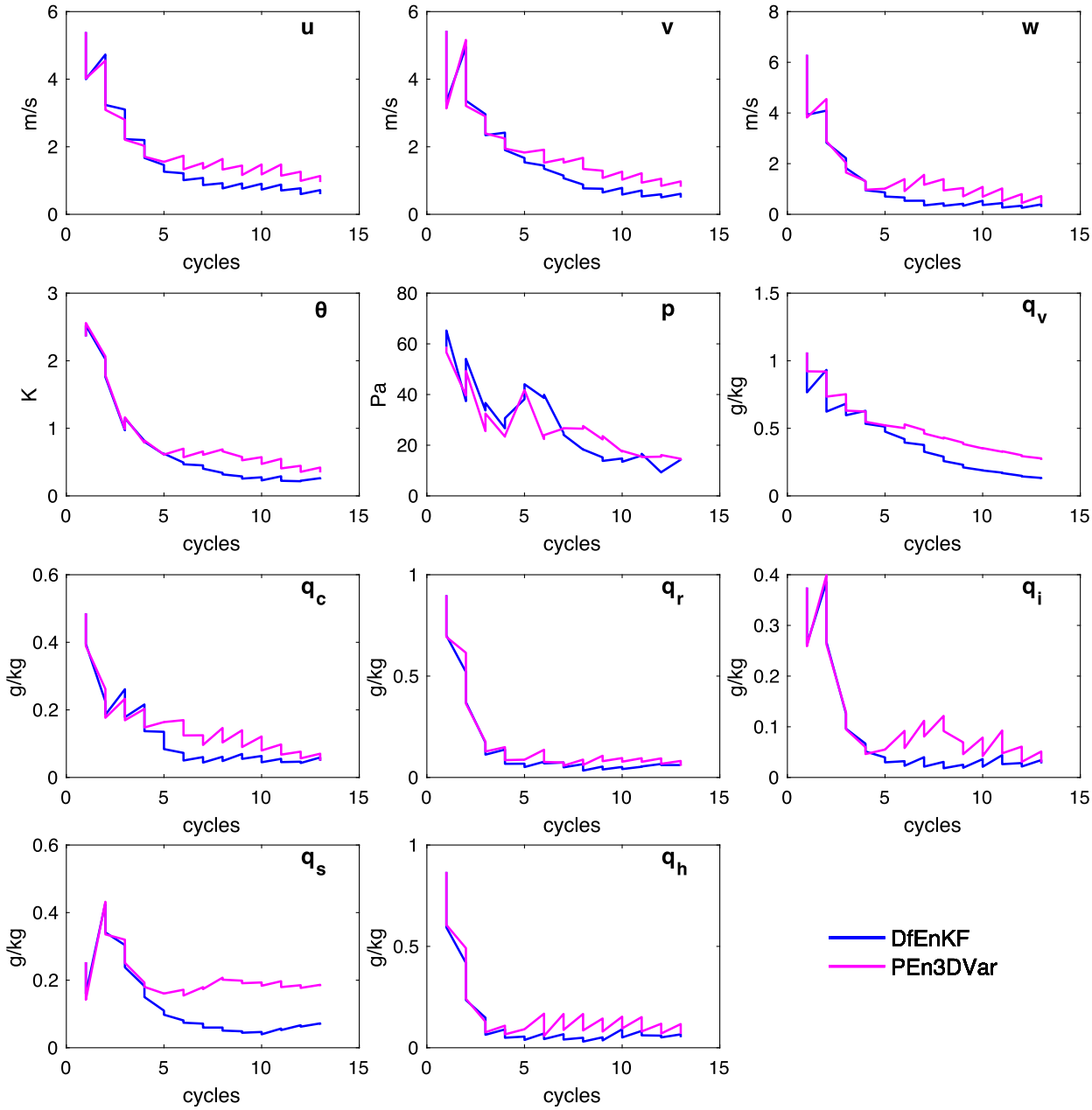

FIG. 5. RMSEs of the background forecasts and analyses of state variables verified in regions with true reflectivity higher than 15 dBZ (solid lines), assimilating both radial velocity and reflectivity data using EnKF (cyan lines), DfEnKF (blue lines), and pure En3DVar (magenta lines) algorithms.

hail at 8 km AGL (the level where the differences between pure En3DVar and DfEnKF are most apparent at the 10th cycle, i.e., 2210 UTC) are depicted in Fig. 6. The spatial extent of the analyzed snow (hail) from pure En3DVar is somewhat underestimated (overestimated), while those from DfEnKF agree better with the truth. The intensities of updraft and downdraft from En3DVar at 8 km AGL are also underestimated while those from DfEnKF are much closer to the truth. Considering that DfEnKF and pure En3DVar use the same background error covariance derived from the EnKF ensemble (at 100% in pure En3DVar), both are based on a deterministic background forecast configured the same way, and the background error covariance localization radii are configured equivalently, the two algorithms should theoretically yield very similar results. Why are the results of En3DVar worse, especially for snow, then? The reasons for the differences will be investigated in detail in the following section.

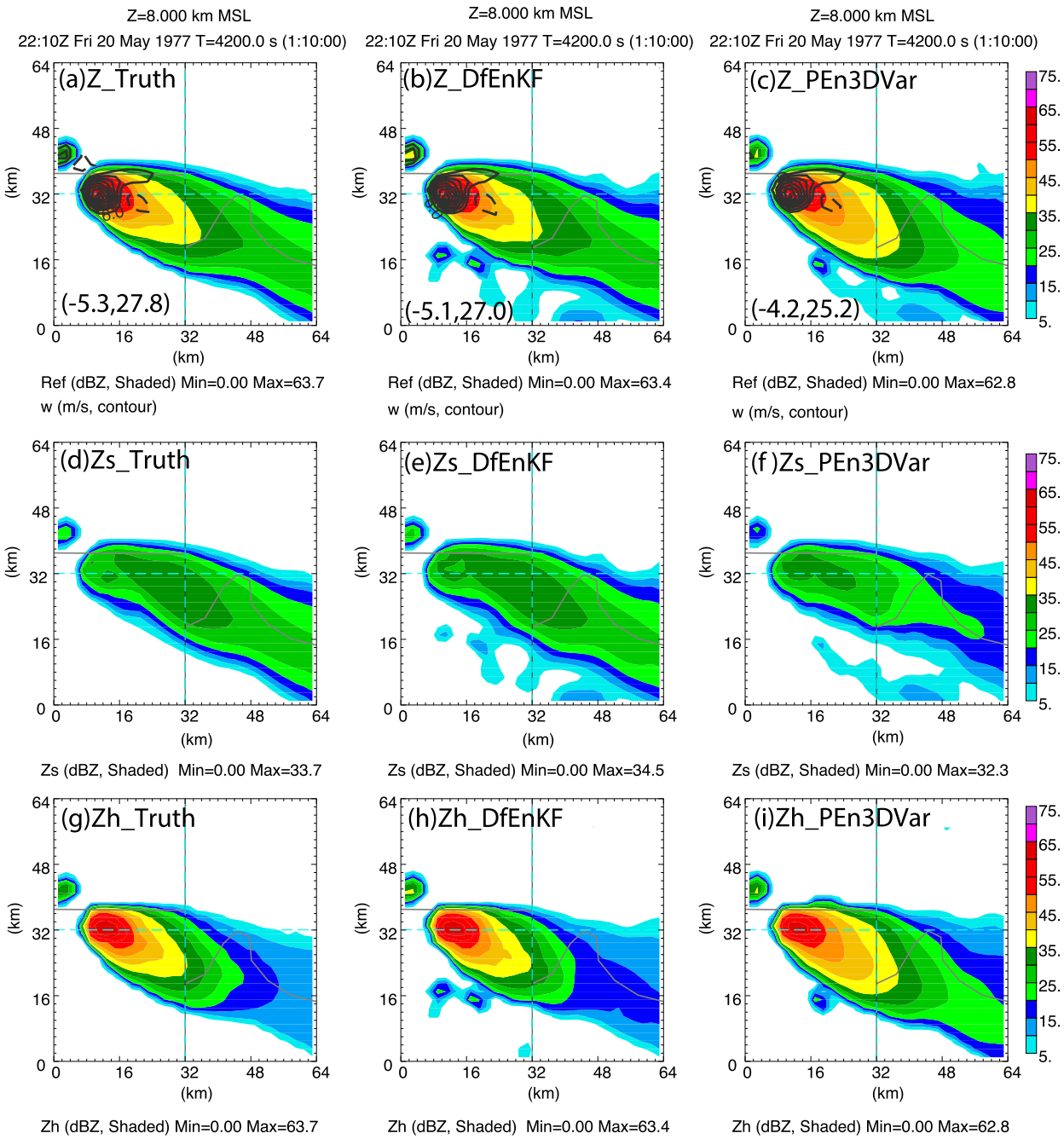

FIG. 6. (left) Truth and analyzed fields at 8 km AGL of (a)–(c) total reflectivity (Z) and reflectivity calculated from mixing ratio of (d)–(f) snow (Zs) and of (g)–(i) hail (Zh) from (middle) DfEnKF and (right) pure En3DVar at the 10th cycle (2210 UTC). Vertical velocity contours are overlaid in the top panels together with the minimum and maximum values.

b. *An analysis of the differences between DfEnKF and pure En3DVar*

Possible reasons for the differences between DfEnKF and pure En3DVar include the following: serial versus global nature of the algorithms, and high nonlinearity of the observational operator of reflectivity that can cause differences between filter update and variational minimization. Sensitivity experiments are conducted to investigate the impact of the above sources.

1) SERIAL VERSUS GLOBAL NATURE OF ALGORITHMS

To compare DfEnKF and pure En3DVar under a linear observation operator condition, only radial velocity

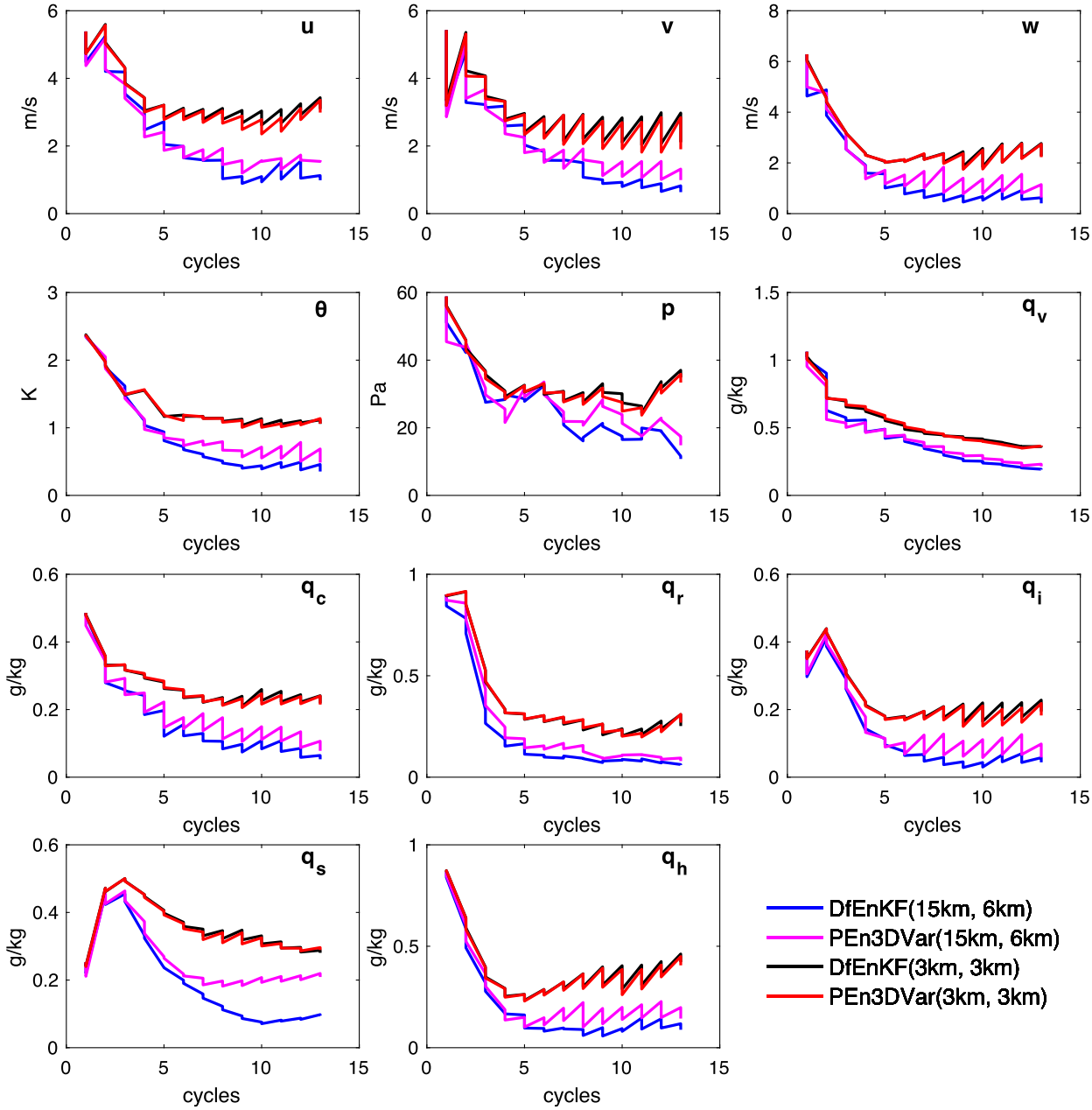

FIG. 7. RMSEs of the forecasts and analyses of state variables verified in regions with true reflectivity higher than 15 dBZ from DfEnKF (blue and black contours) and pure En3DVar (magenta and red contours) when assimilating only radial velocity data with the (horizontal, vertical) localization radii being (15, 6 km) (blue and magenta contours) and (3, 3 km) (black and red contours), respectively.

data are assimilated. In such a case, DfEnKF clearly outperforms pure En3DVar for most of the state variables except for water vapor mixing ratio q_v when using the optimal localization radii of DfEnKF (i.e., 15 km in horizontal and 6 km in vertical) (Fig. 7). The analyses and forecasts of snow mixing ratio in DfEnKF are again better than those of pure En3DVar.

In DfEnKF, the observations are assimilated serially, while observations in En3Dvar are assimilated globally (or simultaneously). To reduce the effect of the order in which data are assimilated, the horizontal (vertical) localization radius is decreased from 15 (6) km to 3 (3) km. This significantly reduces the overlap of the influence regions from neighboring observations (given the 2-km interval of radar data in horizontal and about 1° elevation interval in vertical). When no influence regions from different observations overlap, simultaneous assimilation of all observations should yield the same

result as assimilating one observation at a time, because the assimilation of a prior observation does not affect the assimilation of the following observations.

After significantly decreasing the localization radii, the results of DfEnKF and pure En3DVar become very close (Fig. 7), suggesting the serial versus global nature of the two algorithms is a major cause of the differences in the results of DfEnKF and pure En3DVar when assimilating radial velocity data (for which the observation operator is linear). We point out here that with the reduced non-optimal localization radii, the error levels are clearly higher for all variables than when optimal radii are used (Fig. 7); despite that, data assimilation using either method is still able to decrease error in individual state variables, and the analyzed storm is reasonable (not shown).

2) EFFECTS OF NONLINEAR REFLECTIVITY OBSERVATIONAL OPERATOR IN EN3DVAR AND DFENKF ALGORITHMS

To isolate the effect of nonlinearity in the reflectivity observation operator, only reflectivity data are assimilated in the next set of experiments (Fig. 8). The differences between DfEnKF and pure En3DVar are more obvious compared to the analyses that assimilate radial velocity data only. To reduce the impact of data assimilation sequence, localization radii are again decreased in the same way as earlier for radial velocity data. Unlike the radial velocity case, the differences between DfEnKF and pure En3DVar are still quite obvious even with the reduced localization radii (Fig. 8). This suggests that the nonlinear nature of the reflectivity observation operator is another significant contributor to the differences seen between DfEnKF and pure En3DVar.

To further examine this issue, another single observation test is performed at the time of the second analysis cycle when the analysis differences from the two experiments become large. The background of DfEnKF at the second cycle is used as the background of pure En3DVar also. A single reflectivity observation is placed at a grid point where the analysis difference between DfEnKF and pure En3DVar is most apparent for snow mixing ratio. To better capture the difference, relative error are calculated based on the background, analyzed, and true reflectivity (or equivalent reflectivity) at the given point. The relative error is defined as

$$\eta = \frac{Z^x - Z^t}{Z^t}, \tag{21}$$

where η is the relative error (%), and Z^x is the total reflectivity or equivalent reflectivity for analysis ($x = a$) and forecast ($x = b$), respectively. As is shown in Table 2, the relative error of the background reflectivity at the observation point (Z^b) is 35.2%, which is greatly reduced to 1.8% and 1.9%, respectively, after the assimilation of the single reflectivity data by pure En3DVar and DfEnKF. The relative errors of analyzed equivalent reflectivity (Z_e^a) from pure En3DVar and DfEnKF are 13.6% and 14.3%, respectively, with a small difference of 0.7% only. However, when examining the analyzed equivalent reflectivity components from different hydrometeor species, the relative error differences for snow and hail from DfEnKF and pure En3DVar are much larger (37.0% for Z_e^a of snow and 9.0% for Z_e^a of hail), indicating that the differences in the algorithms are creating significant differences in the analyses of individual hydrometeor fields. Unlike EnKF, for which the analysis is obtained via direct filter update, analysis of En3Dvar is obtained through variational minimization, which tends to adjust hail more than snow because the reflectivity is more sensitive to hail than to snow in the reflectivity observation operator. In variational algorithms, the sensitivity of the cost function to the control variables has a large effect on the amount of adjustment to the individual variables in the minimization process. Variables with small sensitivity may receive little adjustment before the minimization iteration is terminated.

c. *Comparison of hybrid En3DVar with EnKF, DfEnKF, and 3DVar with their optimal configurations*

1) OPTIMAL LOCALIZATION RADII FOR EN3DVAR AND OPTIMAL BACKGROUND ERROR DECORRELATION SCALES FOR 3DVAR

Because of the differences found in the results obtained with DfEnKF and pure En3DVar in the previous sections, the optimal localization radii of DfEnKF are not necessarily the optimal radii of pure En3DVar. To obtain optimal analysis with pure En3DVar, 30 × 20 combinations of horizontal and vertical recursive filter length scales that range from 0.27 to 8.10 km in the horizontal (corresponding to 1- to 30-km cutoff radius of DfEnKF), and from 0.27 to 5.40 km in the vertical (corresponding to 1- to 20-km cutoff radius) are tested to determine the optimal radii in both horizontal and vertical directions. According to the error statistics shown in Fig. 9, the recursive filter length scale of 6.75 km (25-km cutoff) in horizontal and 3.24 km (12-km cutoff) in vertical yield the lowest mean error averaged across all variables. The optimal horizontal cut off radii in terms of the errors of individual fields are close to the overall optimal cutoff radius, but in the vertical direction, the optimal radii for individual fields are either the same or larger than the overall cutoff radii (Fig. 9), although

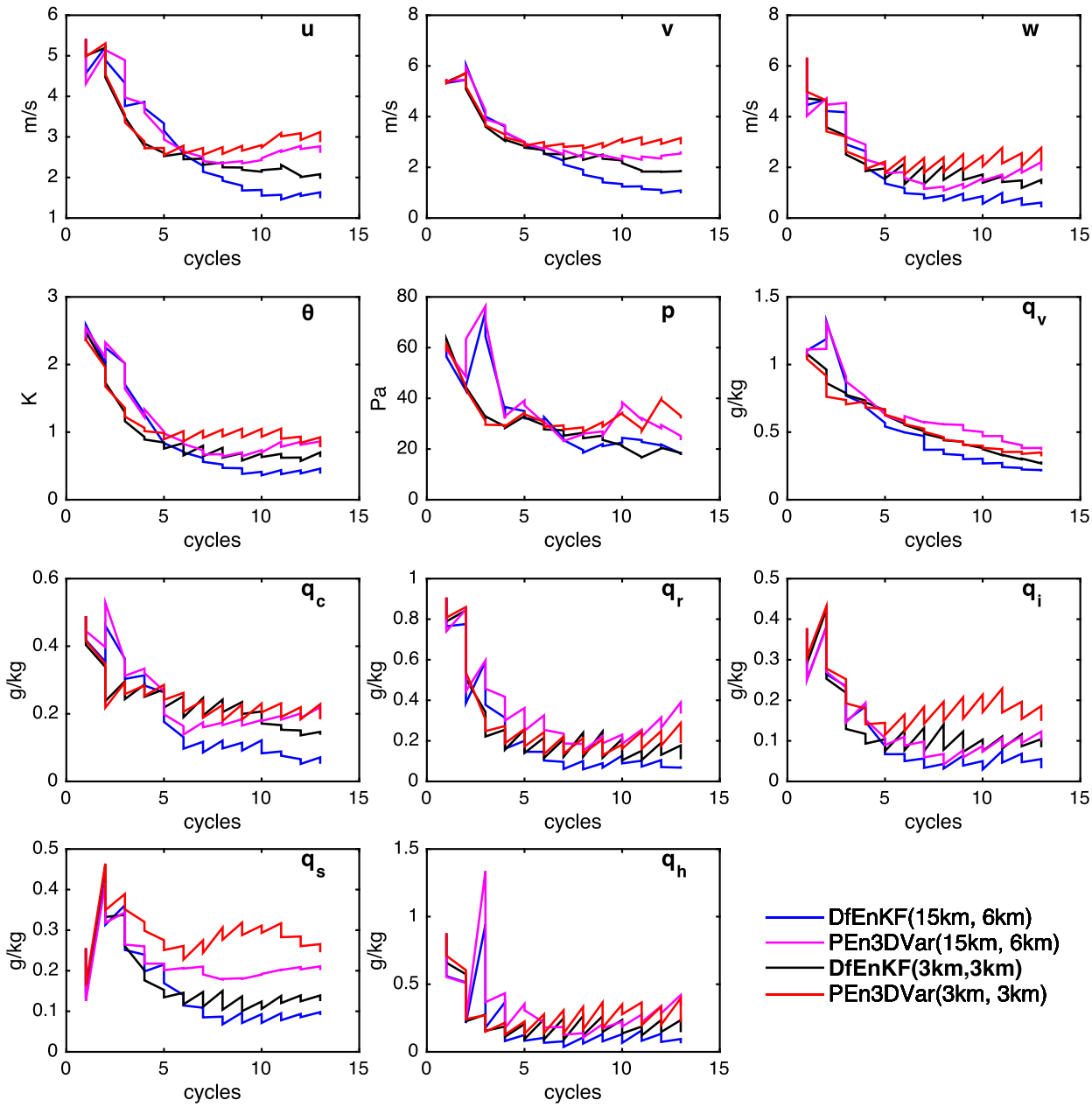

FIG. 8. As in Fig. 7, but when assimilating reflectivity data only.

further error decrease for vertical cutoff radii beyond the overall optimal radius is generally small. In this study, the optimal radii are chosen based on the error averaged across all variables.

The optimal background error decorrelation scales for 3DVar are determined the same way. Background error decorrelation scales are first transformed to cutoff radii of EnKF based on Eq. (19) to keep the experiments of finding optimal cutoff radii (for EnKF) and length scales (for pure En3DVar and 3DVar) more consistent. According to Fig. 10, there is more variation in the optimal scales based on errors of difference variables, especially for the horizontal scale. Based on errors averaged across all variables, background error decorrelation scales of 4.05 km [equivalent to 15-km cutoff based on Eq. (19)] in the horizontal and 1.35 km (5-km cutoff) in the vertical yield the best results. These scales are therefore chosen as the optimal scales for 3DVar experiments.

In the remaining hybrid En3DVar experiments, the optimal localization radii obtained for pure En3DVar and the optimal background error decorrelation scales

TABLE 2. Comparison of single reflectivity observation assimilation between pure En3DVar and DfEnKF. Here Z^t, Z^b, Z^a indicate the true, background, and analyzed reflectivity in dBZ, respectively; Z_e^b, Z_e^a represent the background and analyzed equivalent reflectivity in mm^{6}m^{-3}; and Z_{er}^a, Z_{es}^a, and Z_{eh}^a are the equivalent reflectivity components for rain, snow, and hail, respectively.

	Background or analyzed reflectivity and equivalent reflectivity	Relative error (%) $(Z^x - Z^t)/Z^t, x = a$ or b		Difference of relative error between pure En3DVar and DfEnKF
		Pure En3DVar	DfEnKF	
Background	$Z^b = 10\log_{10}Z_e^b$ (dBZ)	35.17%		0%
Analysis	$Z^a = 10\log_{10}Z_e^a$ (dBZ)	1.78%	1.88%	0.1%
	$Z_e^a = Z_{er}^a + Z_{es}^a + Z_{eh}^a$ (mm^{6}m^{-3})	13.59%	14.26%	0.67%
	Z_{er}^a (mm^{6}m^{-3})	0%	0%	0%
	Z_{es}^a (mm^{6}m^{-3})	54.73%	17.71%	37.02%
	Z_{eh}^a (mm^{6}m^{-3})	4.53%	13.50%	8.97%

obtained for 3DVar will be applied to the flow-dependent ensemble covariance and static covariance, respectively.

2) OPTIMAL HYBRID WEIGHTS AS A FUNCTION OF ENSEMBLE SIZE

To determine the optimal hybrid weights in hybrid En3DVar as a function of ensemble size, 10 × 10 experiments with different combinations of ensemble size (from 10 to 100 with an increment of 10) and the weight given to the static background error covariance (from 0 to 1 with an increment of 0.1) are performed. Pure En3DVar and 3DVar correspond to experiments with the static error weight set to 0 and 1, respectively.

As indicated in Fig. 11, pure 3DVar underperforms both pure and hybrid En3DVar in terms of the largest scaled RMSEs. When the ensemble size is 30 or larger, hybrid En3DVar with a 5%–10% static B performs the best in analyses and forecasts of u, v, θ, p, and q_v (with a couple of exceptions for u and q_v). When the ensemble size is 50 or larger, pure En3DVar (with 0% static B) performs the best in w and all hydrometeor variables. When the ensemble size is only 10 or 20, some variables, including v, θ, cloud water mixing ratio q_c, and q_v, require 50% or larger static weight to achieve the smallest error. For cloud ice mixing ratio q_i, pure En3DVar always has the smallest error.

In terms of the average error across all variables, hybrid En3Dvar with a ~5%–10% (60%) static background error gives the best results when the ensemble size is larger (smaller) than 20. Errors of pure and hybrid En3DVar increase quickly when the ensemble sizes falls below 40. These results indicate that an ensemble size of 30 or larger is needed for the hybrid system to benefit significantly from the ensemble error covariances, and in that case only around 5% of static covariances is beneficial. For variables directly linked to convection (w and hydrometeors), the advantage of static B is not obvious, especially when the ensemble size is 50 or larger.

3) COMPARISONS OF HYBRID EN3DVAR WITH ENKF, DFENKF, AND 3DVAR WITH RESPECTIVE OPTIMAL CONFIGURATIONS

Comparisons are made among the analyses and forecasts from 3DVar, EnKF, DfEnKF, pure, and hybrid En3DVar with their own optimal configurations (including localization/decorrelation scales and covariance weights). In all cases, the ensemble size used is 40, and this choice is guided by the results of section 3c(3), and is also consistent with many of our previous studies with EnKF for radar assimilation (e.g., Xue et al. 2006; Snook et al. 2011). Basically, we want to choose an ensemble size that can produce decent EnKF analyses without excessive costs, and answer the question if their analyses can be further improved by including some static background error via hybrid En3DVar.

The RMSEs are calculated only over grid points where the true reflectivity exceeds 15 dBZ, as have been done earlier. Figure 12 shows that 3DVar performs the worst with RMSEs much larger than others. EnKF and DfEnKF have similar error levels and both outperform pure and hybrid En3DVar for most of the variables in almost all cycles, with the exception being with p in the earlier cycles. As discussed earlier, the pressure analysis is more sensitive to acoustic noise that may affect the reliability of the cross covariance between pressure and radar observations; we therefore give its error less weight in our performance assessment. Among the variables, q_v seems to benefit from the hybrid covariance the most as the error levels of hybrid En3DVar are lower than pure En3DVar and close to EnKF (and DfEnKF). The difference between EnKF (or DfEnKF) and pure (or hybrid) En3DVar is the largest for q_s. As discussed in section 3b, their differences are mainly caused by the serial versus global nature of the algorithms and the variational minimization versus direct filter updating (which is sensitive to nonlinearity). In a variational framework, it is much more difficult to adjust mixing ratio of dry snow by reflectivity assimilation because the gradient of the reflectivity

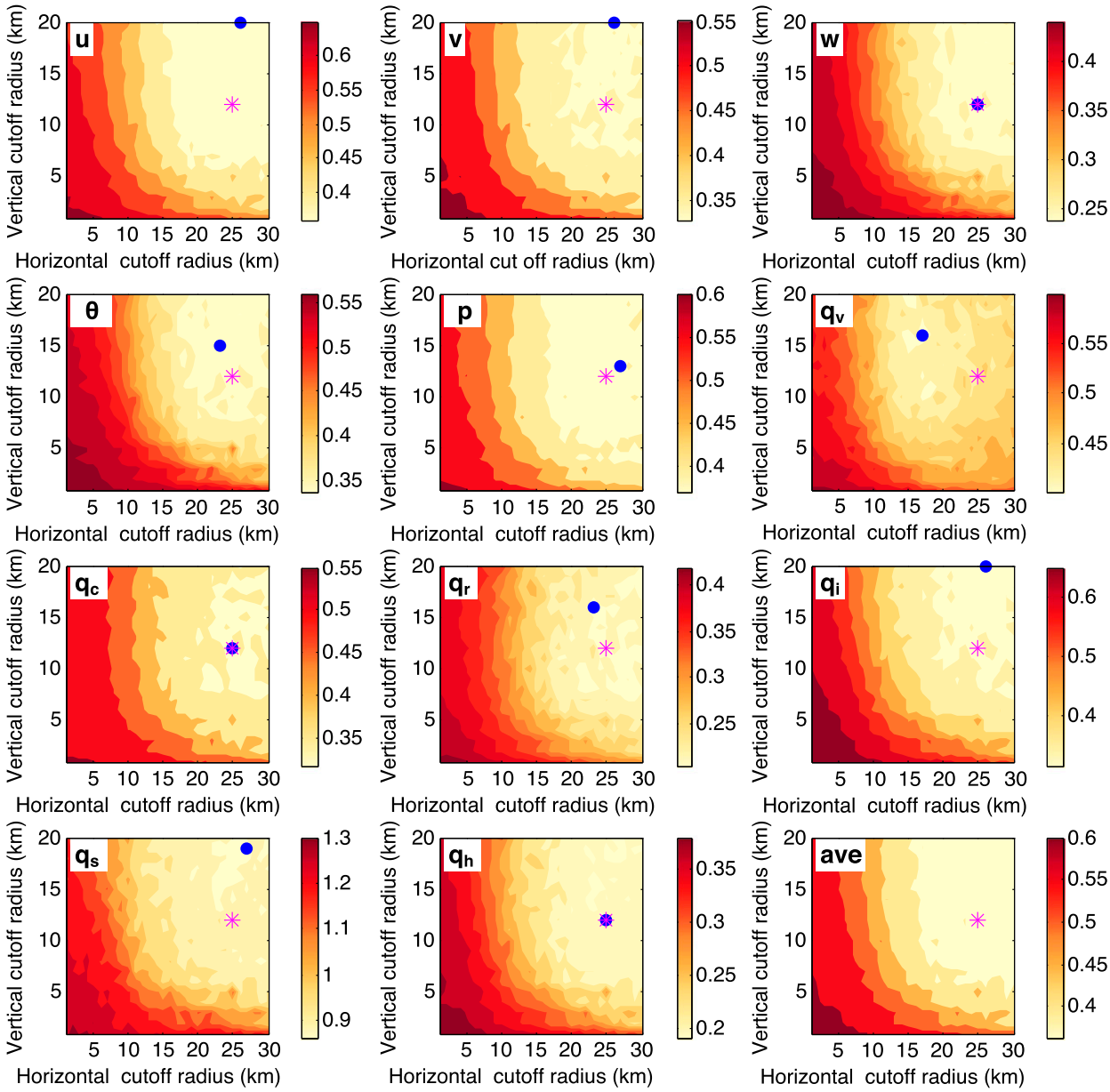

FIG. 9. The mean scaled RMSEs as defined in Eq. (18) for different state variables and averaged over all variables (ave), which are obtained based on pure En3DVar experiments with 30 × 20 combinations of horizontal and vertical length scales after being transformed to cutoff radii of EnKF based on Eq. (19). The blue dot in each panel indicates the location of minimum scaled RMSE for the corresponding variable and the magenta asterisk indicates the minimum value across all the variables.

operator to dry snow is much smaller than those to hail and rain. In other words, when hail and dry snow coexist, the adjustment to hail tends to dominate, making correction to errors in dry snow more difficult.

Vertical cross sections of analyzed reflectivity and winds from 3DVar, EnKF, DfEnKF, and pure and hybrid En3DVar after 1-h of DA cycles are shown in Fig. 13 together with the truth. The maximum reflectivity analyses from 3DVar and hybrid En3DVar are 67.7 and 70.3 dBZ, which are less than those from the truth and EnKF (about 71 dBZ), indicating that both hybrid En3DVar and 3DVar underestimate the intensity of the reflectivity core (e.g., reflectivity exceeding 70 dBZ). The maximum vertical velocity from EnKF, DfEnKF, and pure and hyrbrid En3DVar are over 25 m s^{-1}, which are much larger than that from 3DVar (18.8 m s^{-1}) and closer to that of the truth (27.1 m s^{-1}). Some spurious reflectivity is found outside the truth storm region in the analyses of 3DVar and hybrid

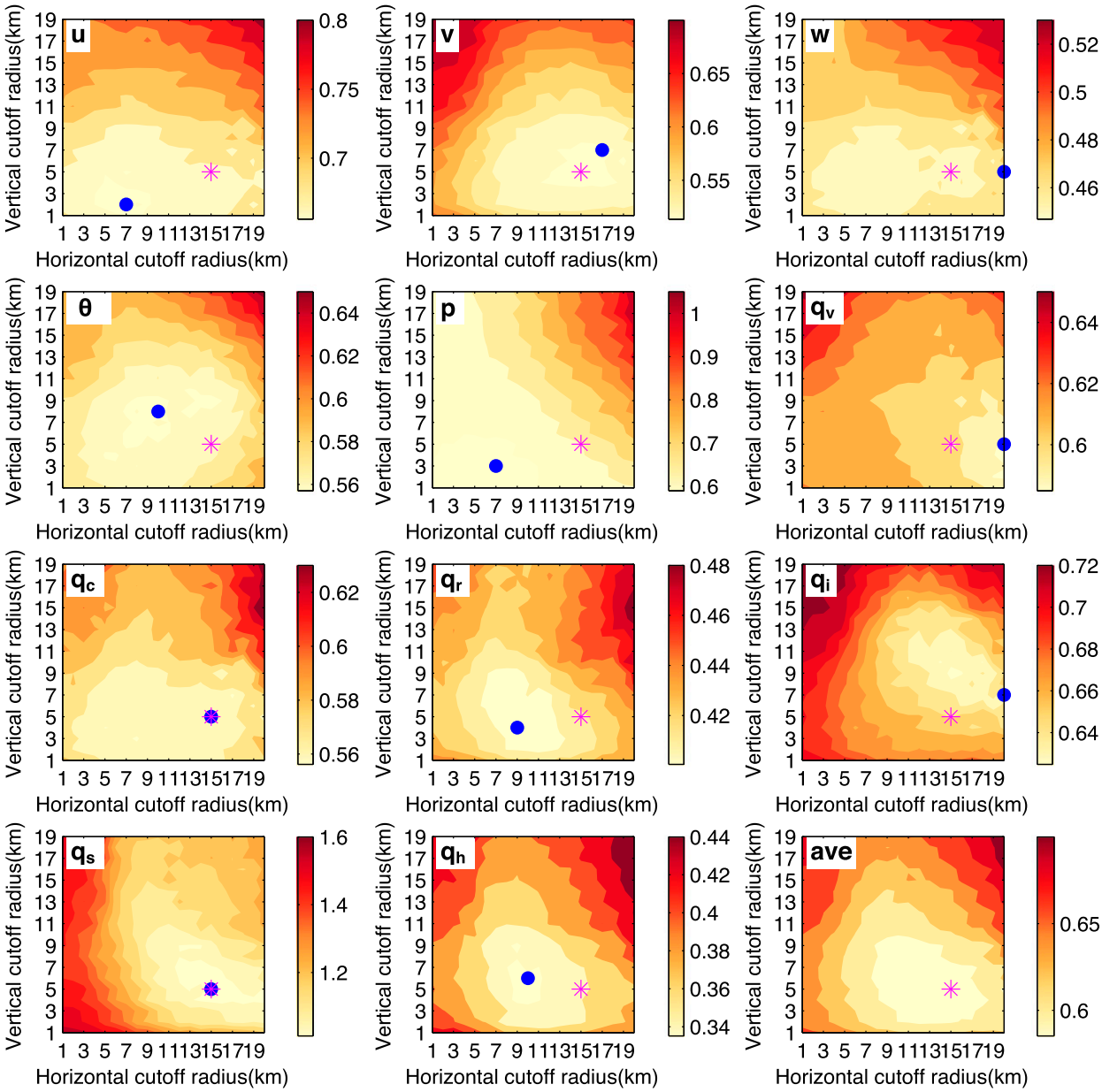

FIG. 10. The mean scaled RMSEs as defined in Eq. (18) for different state variables and averaged over all variables (ave), which are obtained based on 3DVar experiments with 20 × 20 combinations of horizontal and vertical decorrelation length scales after being transformed to EnKF's cutoff radii based on Eq. (19) (to be consistent with Fig. 9). The blue dot in each panel indicates the location of minimum scaled RMSE for the corresponding variable and the magenta asterisk indicates the minimum value across all the variables.

En3DVar, which can be caused by the assimilation of error-containing reflectivity observations (whose errors can exceed 3 dBZ). In EnKF, DfEnKF, and pure En3DVar, spurious perturbations in the background forecasts can be effectively suppressed through flow-dependent background error correlations if zero reflectivity is assimilated, as was pointed out by Tong and Xue (2005).

To examine the quality of analyzed hydrometeor fields, we compare the reflectivity components from individual hydrometeor mixing ratios according to Eq. (20). According to Fig. 14, the contribution to equivalent reflectivity from analyzed rainwater mixing ratio q_r from different algorithms are very similar and close to that of truth. For hail, 3DVar and hybrid En3DVar underestimate the hail reflectivity at the reflectivity core region, contributing to the underestimation of maximum analyzed total reflectivity noted earlier. For snow, EnKF and DfEnKF obtain

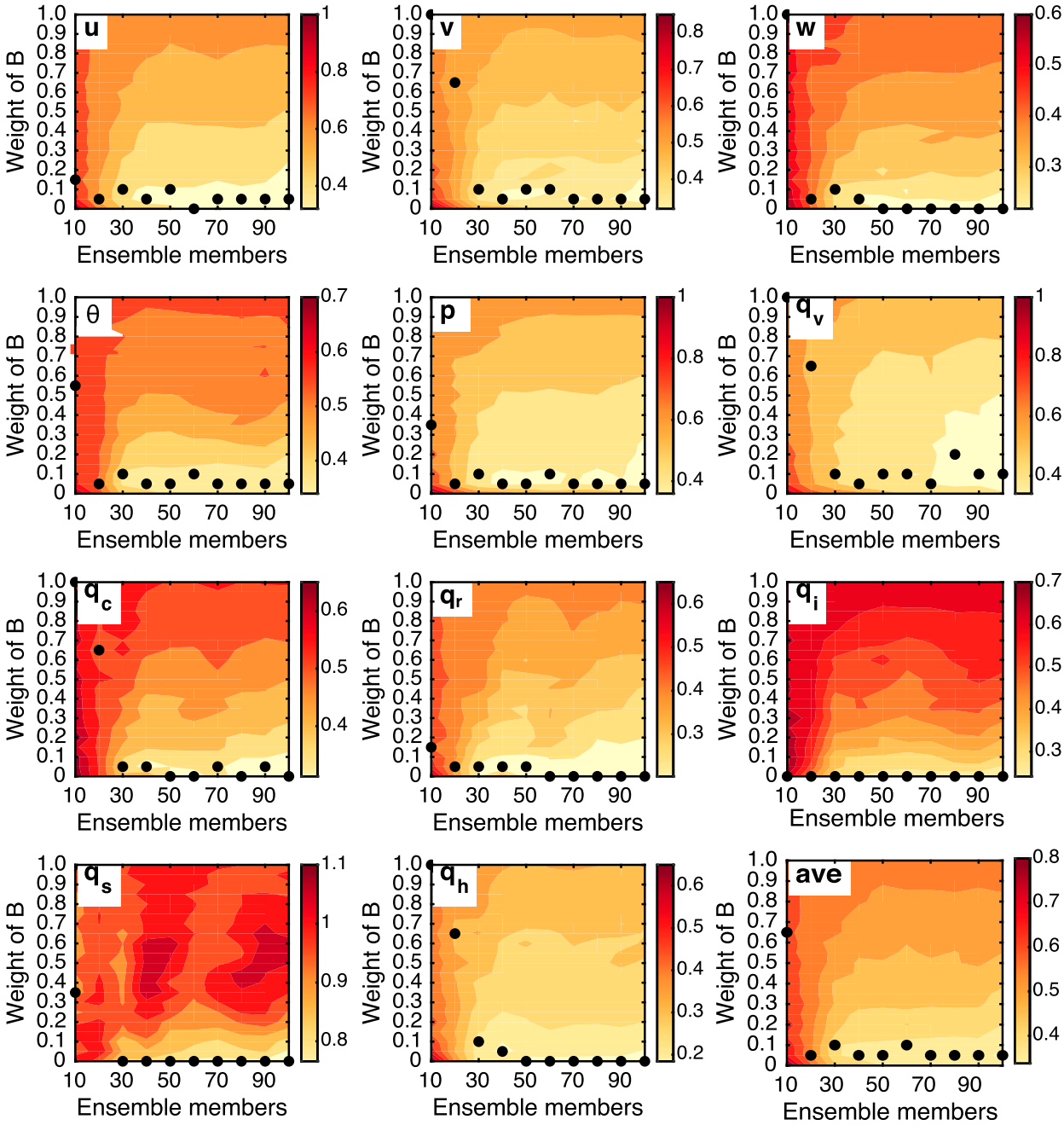

FIG. 11. The gridpoint average of the scaled RMSEs as defined in Eq. (18) for different variables and averaged over all variables (ave), which are obtained based on hybrid En3DVar experiments with different combinations of ensemble sizes and hybrid weights. The black dots indicate locations of the optimal weights for different ensemble sizes.

better analyses than pure En3DVar, hybrid En3DVar, and 3DVar. The contribution of snow to total reflectivity is, however, much smaller than that of hail, making correction to its error more difficult in a variational framework.

Overall, EnKF, DfEnKF, and pure En3DVar give similar reflectivity or precipitating hydrometeor analyses that are very close to truth. There is some benefit to bring in 5% or so static error covariance into En3DVar to form a hybrid algorithm when verified within precipitation regions, but some spurious reflectivity can appear in the clear-air regions (Fig. 14) that can degrade the overall analyses, similar to the 3DVar case.

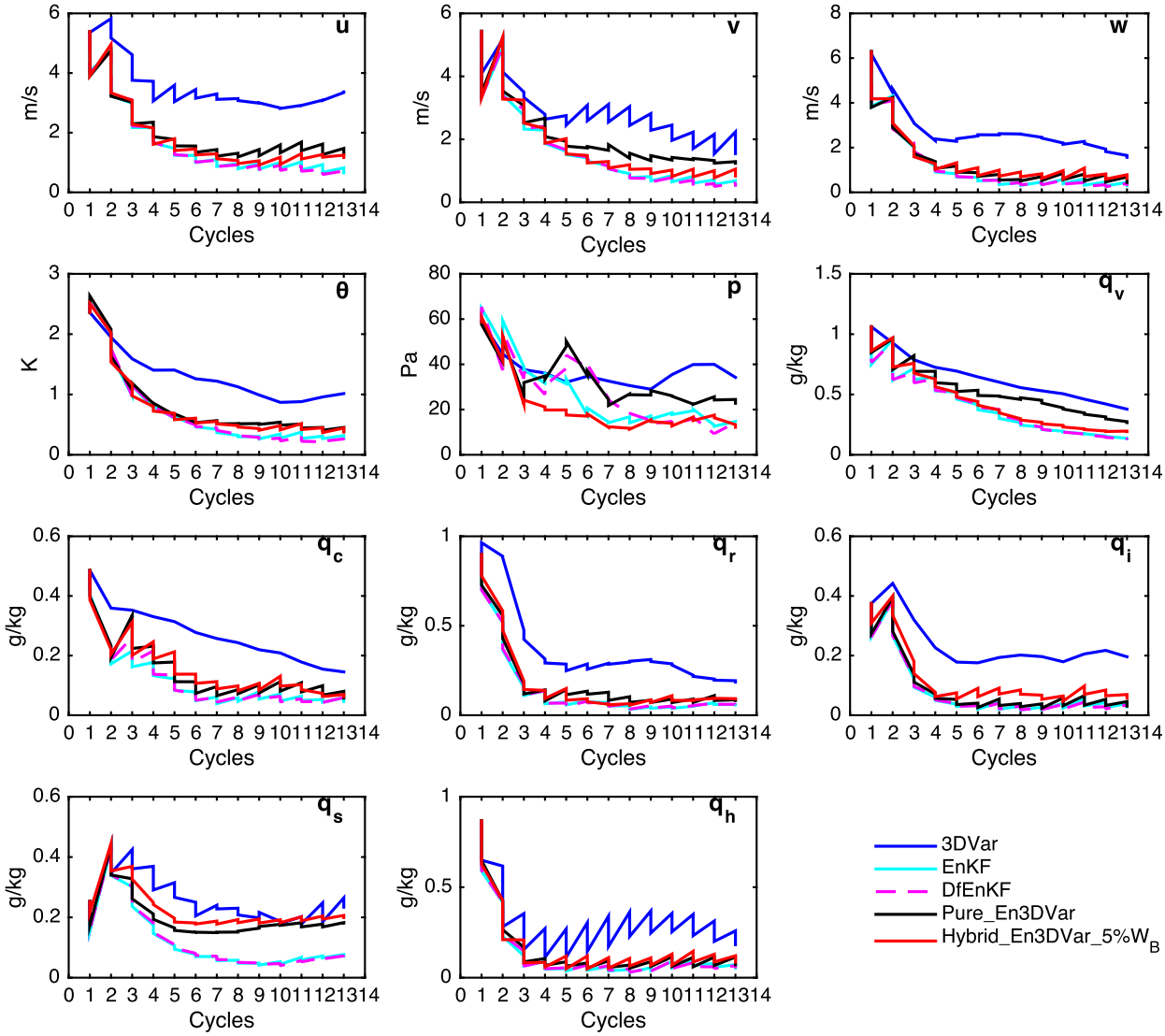

FIG. 12. The gridpoint average of the RMSEs over the region where true reflectivity is higher than 15 dBZ for 3DVar, EnKF, DfEnKF, and pure and hybrid En3DVar (5% weight given to static B).

4. Summary and conclusions

In this study, a hybrid En3DVar system was developed based on the ARPS variational framework and is applied to the assimilation of simulated radar data for a supercell storm. Radar radial velocity and reflectivity data were assimilated every 5 min for 1 h. Differences between EnKF and pure En3DVar are first investigated to better understand the difference among different algorithms. DfEnKF, which updates a single deterministic background forecast using the EnKF mean updating algorithm, is introduced to have an algorithm-wise parallel comparison between EnKF and pure En3DVar. 3DVar, EnKF, DfEnKF, and pure and hybrid En3DVar are tuned to obtain their optimal configurations before they are compared. The experiments performed and related conclusions are summarized as follows:

- Single-point radial velocity or reflectivity data assimilation experiments show that pure En3DVar and DfEnKF produce similar flow-dependent analysis increments that depict flow-dependent structures while 3DVar produces isotropic analysis increments that are not necessarily physical.
- Differences are found in the analyses of DfEnKF and pure En3DVar when both use the same effective localization scales even though they are supposed to be the same for linear and Gaussian problems. The serial versus global nature of the algorithm is shown to be responsible for the analysis differences when assimilating

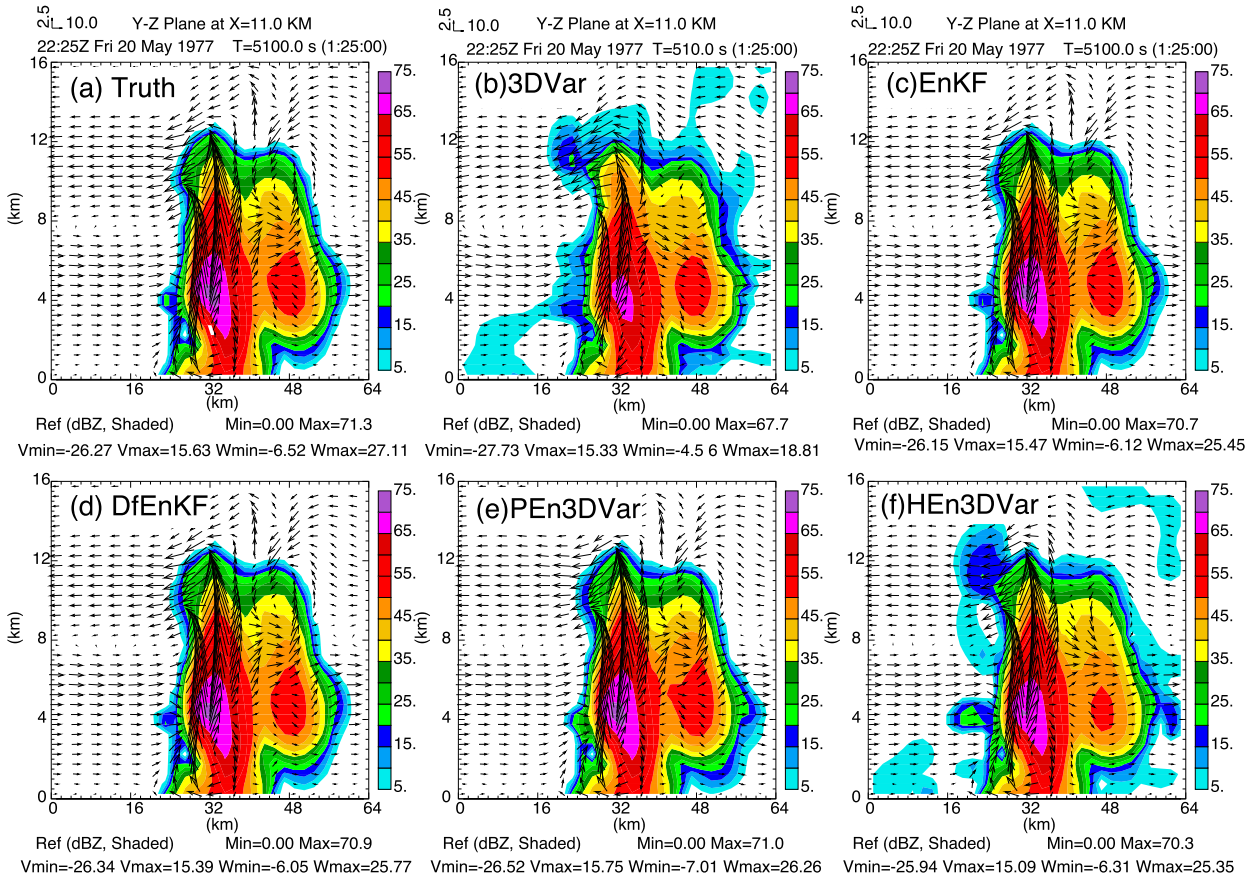

FIG. 13. Vertical cross sections of the reflectivity field overlaid with the wind vector at the end of the 1-h DA window from (a) truth, and the analyses of (b) 3DVar, (c) pure En3DVar, (d) DfEnKF, (e) pure En3DVar, and (f) hybrid En3DVar with 5% static covariance.

radial velocity whose observation operator is linear. The variational minimization versus direct filter update nature of the algorithms is responsible for the analysis differences when assimilating reflectivity whose observation operator is highly nonlinear. As a variational algorithm, pure En3DVar tends to adjust hail more than snow, because the analysis results are controlled to a large extent by the sensitivity of reflectivity with respect to individual hydrometeor (i.e., the gradient of the reflectivity operator with respect to the hydrometeor state variables). The EnKF/DfEnKF algorithm relies on the background error covariances for analysis updating.

- For 3DVar, optimal decorrelation scales for static background error covariances are obtained via sensitivity experiments, and the optimal localization radii for ensemble background error covariances are similarly obtained for EnKF/DfEnKF and En3DVar. These optimal configurations are then used to construct hybrid En3DVar. The sensitivity of hybrid En3DVar to covariance weights and ensemble size is then examined.
- It is found that when the ensemble size is 30 or larger, a 5%–10% weight for static covariance produces the smallest mean errors for u, v, θ, p, and q_v fields. For w and hydrometeor fields, 0% static covariance performs the best when the ensemble size is 50 or larger. On average, when the ensemble size is 20 or larger, a 5% or 10% static covariance gives the best results while for smaller ensembles a larger static covariance with a ~50% weight produces somewhat better results. Using an ensemble size of 40, EnKF and DfEnKF perform similarly, and both are better than pure and hybrid En3DVar overall. Using 5% static error covariance, hybrid En3DVar outperforms pure En3DVar for most variables except the hydrometeor variables; the improvement is the largest for q_v and the degradation is most notable for q_s. In a sense, the extra static error covariance does not help for hydrometeor variables. Overall, in the current perfect OSSE framework, EnKF and DfEnKF perform similarly and are the best, while 3DVar performs the worst. En3DVar with or without static background error covariance does not perform as well as EnKF/DfEnKF, and static covariance only helps slightly via hybrid En3DVar.

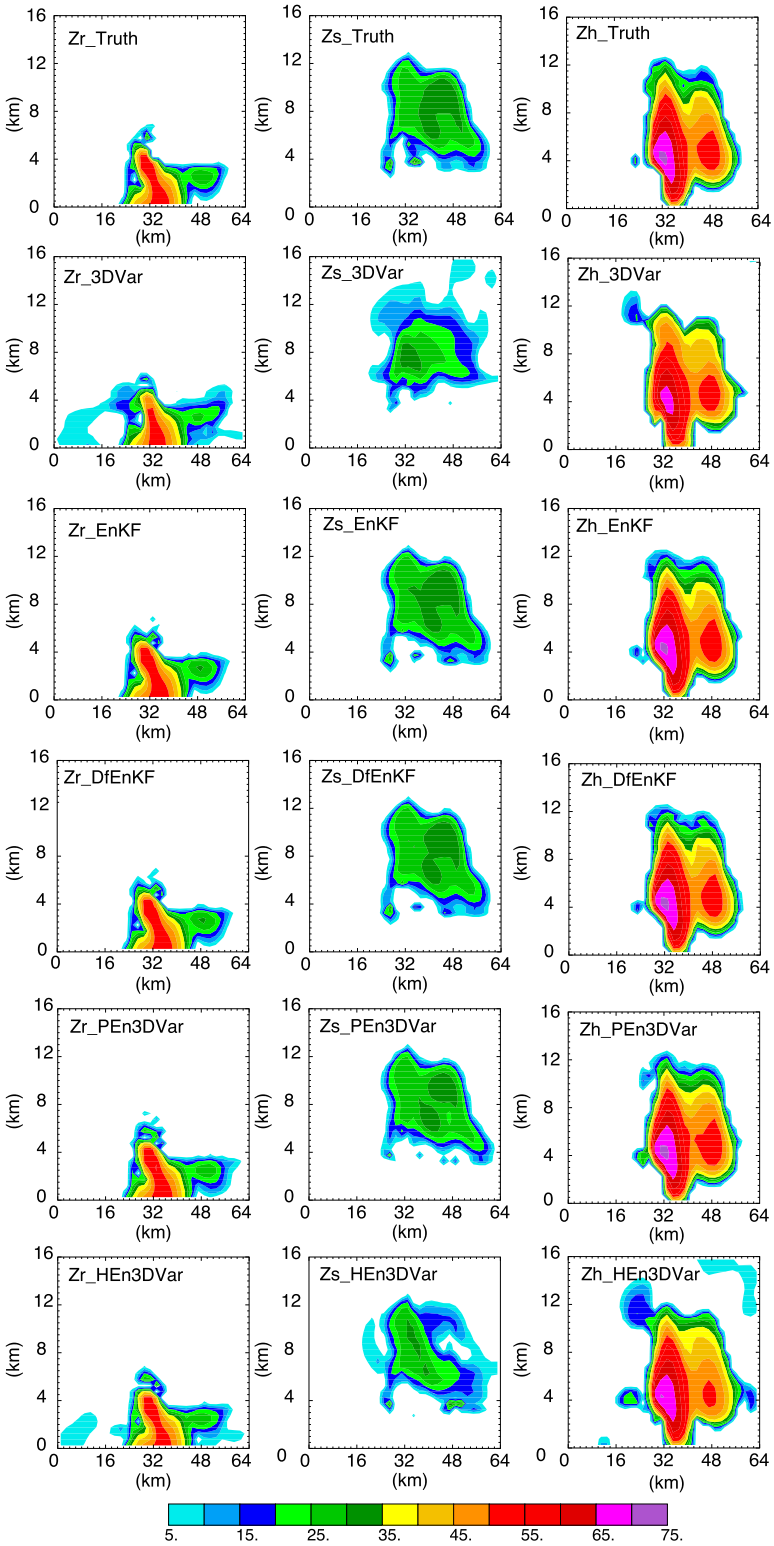

FIG. 14. Vertical cross sections of the reflectivity (in dBZ) calculated based on the mixing ratio analyses of rain (Zr), snow (Zs), and hail (Zh) from truth, analyses of 3DVar, EnKF, DfEnKF, and pure and hybrid En3DVar, respectively.

Finally, we note that the conclusions obtained here are based on the assumption of a perfect prediction model. In the future, we will compare hybrid En3DVar against EnKF and 3DVar under imperfect-model conditions and will apply the algorithms to real cases afterward.

Acknowledgments. This research was primarily supported by the NOAA Warn-on-Forecast (WoF) Grant NA160AR4320115. The second author was also supported by NSF Grants AGS-0941491 and AGS-1046171. Dr. Louis Wicker of NSSL is thanked for reviewing the manuscript and for his support within the WoF project. The reviews by three anonymous reviewers also helped improved our paper. Computational resources of the Oklahoma Supercomputing Center for Research and Education (OSCER), and the NSF Xsede Supercomputing Centers were used.

REFERENCES

Aksoy, A., D. C. Dowell, and C. Snyder, 2009: A multicase comparative assessment of the ensemble Kalman filter for assimilation of radar observations. Part I: Storm-scale analyses. *Mon. Wea. Rev.*, **137**, 1805–1824, https://doi.org/10.1175/2008MWR2691.1.

——, ——, and ——, 2010: A multicase comparative assessment of the ensemble Kalman filter for assimilation of radar observations. Part II: Short-range ensemble forecasts. *Mon. Wea. Rev.*, **138**, 1273–1292, https://doi.org/10.1175/2009MWR3086.1.

Buehner, M., P. L. Houtekamer, C. Charette, H. L. Mitchell, and B. He, 2010a: Intercomparison of variational data assimilation and the ensemble Kalman filter for global deterministic NWP. Part I: Description and single-observation experiments. *Mon. Wea. Rev.*, **138**, 1550–1566, https://doi.org/10.1175/2009MWR3157.1.

——, ——, ——, ——, and ——, 2010b: Intercomparison of variational data assimilation and the ensemble Kalman filter for global deterministic NWP. Part II: One-month experiments with real observations. *Mon. Wea. Rev.*, **138**, 1567–1586, https://doi.org/10.1175/2009MWR3158.1.

——, J. Morneau, and C. Charette, 2013: Four-dimensional ensemble-variational data assimilation for global deterministic weather prediction. *Nonlinear Processes Geophys.*, **20**, 669–682, https://doi.org/10.5194/npg-20-669-2013.

Clayton, A. M., A. C. Lorenc, and D. M. Barker, 2013: Operational implementation of a hybrid ensemble/4D-Var global data assimilation system at the Met Office. *Quart. J. Roy. Meteor. Soc.*, **139**, 1445–1461, https://doi.org/10.1002/qj.2054.

Dowell, D. C., F. Q. Zhang, L. J. Wicker, C. Snyder, and N. A. Crook, 2004: Wind and temperature retrievals in the 17 May 1981 Arcadia, Oklahoma, supercell: Ensemble Kalman filter experiments. *Mon. Wea. Rev.*, **132**, 1982–2005, https://doi.org/10.1175/1520-0493(2004)132<1982:WATRIT>2.0.CO;2.

——, L. J. Wicker, and C. Snyder, 2011: Ensemble Kalman filter assimilation of radar observations of the 8 May 2003 Oklahoma City supercell: Influences of reflectivity observations on storm-scale analyses. *Mon. Wea. Rev.*, **139**, 272–294, https://doi.org/10.1175/2010MWR3438.1.

Etherton, B. J., and C. H. Bishop, 2004: Resilience of hybrid ensemble/3DVAR analysis schemes to model error and ensemble covariance error. *Mon. Wea. Rev.*, **132**, 1065–1080, https://doi.org/10.1175/1520-0493(2004)132<1065:ROHDAS>2.0.CO;2.

Gao, J. D., M. Xue, A. Shapiro, and K. K. Droegemeier, 1999: A variational method for the analysis of three-dimensional wind fields from two Doppler radars. *Mon. Wea. Rev.*, **127**, 2128–2142, https://doi.org/10.1175/1520-0493(1999)127<2128:AVMFTA>2.0.CO;2.

——, ——, K. Brewster, and K. K. Droegemeier, 2004: A three-dimensional variational data analysis method with recursive filter for Doppler radars. *J. Atmos. Oceanic Technol.*, **21**, 457–469, https://doi.org/10.1175/1520-0426(2004)021<0457:ATVDAM>2.0.CO;2.

——, ——, and D. J. Stensrud, 2013: The development of a hybrid EnKF-3DVAR algorithm for storm-scale data assimilation. *Adv. Meteor.*, **2013**, 512656, https://doi.org/10.1155/2013/512656.

——, D. J. Stensrud, L. Wicker, M. Xue, and K. Zhao, 2014: Storm-scale radar data assimilation and high resolution NWP. *Adv. Meteor.*, **2014**, 213579, https://doi.org/10.1155/2014/213579.

——, C. Fu, D. J. Stensrud, and J. S. Kain, 2016: OSSEs for an ensemble 3DVAR data assimilation system with radar observations of convective storms. *J. Atmos. Sci.*, **73**, 2403–2426, https://doi.org/10.1175/JAS-D-15-0311.1.

Gaspari, G., and S. E. Cohn, 1999: Construction of correlation functions in two and three dimensions. *Quart. J. Roy. Meteor. Soc.*, **125**, 723–757, https://doi.org/10.1002/qj.49712555417.

Greybush, S. J., E. Kalnay, T. Miyoshi, K. Ide, and B. R. Hunt, 2011: Balance and ensemble Kalman filter localization techniques. *Mon. Wea. Rev.*, **139**, 511–522, https://doi.org/10.1175/2010MWR3328.1.

Hamill, T. M., and C. Snyder, 2000: A hybrid ensemble Kalman filter–3D variational analysis scheme. *Mon. Wea. Rev.*, **128**, 2905–2919, https://doi.org/10.1175/1520-0493(2000)128<2905:AHEKFV>2.0.CO;2.

——, ——, and R. E. Morss, 2000: A comparison of probabilistic forecasts from bred, singular-vector, and perturbed observation ensembles. *Mon. Wea. Rev.*, **128**, 1835–1851, https://doi.org/10.1175/1520-0493(2000)128<1835:ACOPFF>2.0.CO;2.

——, J. S. Whitaker, and C. Snyder, 2001: Distance-dependent filtering of background error covariance estimates in an ensemble Kalman filter. *Mon. Wea. Rev.*, **129**, 2776–2790, https://doi.org/10.1175/1520-0493(2001)129<2776:DDFOBE>2.0.CO;2.

Houtekamer, P. L., and H. L. Mitchell, 1998: Data assimilation using an ensemble Kalman filter technique. *Mon. Wea. Rev.*, **126**, 796–811, https://doi.org/10.1175/1520-0493(1998)126<0796:DAUAEK>2.0.CO;2.

——, and ——, 2005: Ensemble Kalman filtering. *Quart. J. Roy. Meteor. Soc.*, **131**, 3269–3289, https://doi.org/10.1256/qj.05.135.

Hu, M., M. Xue, and K. Brewster, 2006a: 3DVAR and cloud analysis with WSR-88D level-II data for the prediction of the Fort Worth, Texas, tornadic thunderstorms. Part I: Cloud analysis and its impact. *Mon. Wea. Rev.*, **134**, 675–698, https://doi.org/10.1175/MWR3092.1.

——, ——, J. D. Gao, and K. Brewster, 2006b: 3DVAR and cloud analysis with WSR-88D level-II data for the prediction of the Fort Worth, Texas, tornadic thunderstorms. Part II: Impact of radial velocity analysis via 3DVAR. *Mon. Wea. Rev.*, **134**, 699–721, https://doi.org/10.1175/MWR3093.1.

Jung, Y. S., M. Xue, G. F. Zhang, and J. M. Straka, 2008: Assimilation of simulated polarimetric radar data for a convective storm using the ensemble Kalman filter. Part II: Impact of polarimetric data on storm analysis. *Mon. Wea. Rev.*, **136**, 2246–2260, https://doi.org/10.1175/2007MWR2288.1.

Kain, J. S., and Coauthors, 2010: Assessing advances in the assimilation of radar data and other mesoscale observations within a collaborative forecasting–research environment. *Wea. Forecasting*, **25**, 1510–1521, https://doi.org/10.1175/2010WAF2222405.1.

Kepert, J. D., 2009: Covariance localisation and balance in an ensemble Kalman filter. *Quart. J. Roy. Meteor. Soc.*, **135**, 1157–1176, https://doi.org/10.1002/qj.443.

Li, Y. Z., X. H. Wang, and M. Xue, 2012: Assimilation of radar radial velocity data with the WRF hybrid ensemble–3DVAR system for the prediction of Hurricane Ike (2008). *Mon. Wea. Rev.*, **140**, 3507–3524, https://doi.org/10.1175/MWR-D-12-00043.1.

Lin, Y. L., R. D. Farley, and H. D. Orville, 1983: Bulk parameterization of the snow field in a cloud model. *J. Climate Appl. Meteor.*, **22**, 1065–1092, https://doi.org/10.1175/1520-0450(1983)022<1065:BPOTSF>2.0.CO;2.

Liu, C. S., and M. Xue, 2016: Relationships among four-dimensional hybrid ensemble-variational data assimilation algorithms with full and approximate ensemble covariance localization. *Mon. Wea. Rev.*, **144**, 591–606, https://doi.org/10.1175/MWR-D-15-0203.1.

——, ——, and R. Kong, 2016: Assimilation of reflectivity data within the APRS hybrid three-dimensional ensemble-variational (3DEnVar) data assimilation framework. *Seventh EnKF Data Assimilation Workshop*, State College, PA, http://www.adapt.psu.edu/2016EnKFWorkshop/ABSTRACTS/Chengsi_Liu_oral.html.

Lorenc, A. C., 2003: The potential of the ensemble Kalman filter for NWP—A comparison with 4D-Var. *Quart. J. Roy. Meteor. Soc.*, **129**, 3183–3203, https://doi.org/10.1256/qj.02.132.

Pan, Y. J., K. Zhu, M. Xue, X. Wang, M. Hu, S. G. Benjamin, S. S. Weygandt, and J. S. Whitaker, 2014: A GSI-based coupled EnSRF-En3DVar hybrid data assimilation system for the operational rapid refresh model: Tests at a reduced resolution. *Mon. Wea. Rev.*, **142**, 3756–3780, https://doi.org/10.1175/MWR-D-13-00242.1.

Ray, P. S., B. Johnson, K. Johnson, J. Bradberry, J. Stephens, K. Wagner, R. Wilhelmson, and J. Klemp, 1981: The morphology of several tornadic storms on 20 May 1977. *J. Atmos. Sci.*, **38**, 1643–1663, https://doi.org/10.1175/1520-0469(1981)038<1643:TMOSTS>2.0.CO;2.

Sakov, P., and P. R. Oke, 2008: A deterministic formulation of the ensemble Kalman filter: An alternative to ensemble square root filters. *Tellus*, **60A**, 361–371, https://doi.org/10.1111/j.1600-0870.2007.00299.x.

Snook, N., M. Xue, and Y. S. Jung, 2011: Analysis of a tornadic mesoscale convective vortex based on ensemble Kalman filter assimilation of CASA X-Band and WSR-88D radar data. *Mon. Wea. Rev.*, **139**, 3446–3468, https://doi.org/10.1175/MWR-D-10-05053.1.

——, ——, and ——, 2015: Multiscale EnKF assimilation of radar and conventional observations and ensemble forecasting for a tornadic mesoscale convective system. *Mon. Wea. Rev.*, **143**, 1035–1057, https://doi.org/10.1175/MWR-D-13-00262.1.

Snyder, C., and F. Q. Zhang, 2003: Assimilation of simulated Doppler radar observations with an ensemble Kalman filter. *Mon. Wea. Rev.*, **131**, 1663–1677, https://doi.org/10.1175//2555.1.

Sobash, R. A., and D. J. Stensrud, 2013: The impact of covariance localization for radar data on EnKF analyses of a developing MCS: Observing system simulation experiments. *Mon. Wea. Rev.*, **141**, 3691–3709, https://doi.org/10.1175/MWR-D-12-00203.1.

Stensrud, D. J., and Coauthors, 2013: Progress and challenges with warn-on-forecast. *Atmos. Res.*, **123**, 2–16, https://doi.org/10.1016/j.atmosres.2012.04.004.

Sun, J. Z., and Coauthors, 2014: Use of NWP for nowcasting convective precipitation: Recent progress and challenges. *Bull. Amer. Meteor. Soc.*, **95**, 409–426, https://doi.org/10.1175/BAMS-D-11-00263.1.

Tong, M. J., and M. Xue, 2005: Ensemble Kalman filter assimilation of Doppler radar data with a compressible nonhydrostatic model: OSS Experiments. *Mon. Wea. Rev.*, **133**, 1789–1807, https://doi.org/10.1175/MWR2898.1.

——, and ——, 2008: Simultaneous estimation of microphysical parameters and atmospheric state with simulated radar data and ensemble square root Kalman filter. Part I: Sensitivity analysis and parameter identifiability. *Mon. Wea. Rev.*, **136**, 1630–1648, https://doi.org/10.1175/2007MWR2070.1.

Wang, X. G., T. A. Hamill, J. S. Whitaker, and C. H. Bishop, 2007: A comparison of hybrid ensemble transform Kalman filter-optimum interpolation and ensemble square root filter analysis schemes. *Mon. Wea. Rev.*, **135**, 1055–1076, https://doi.org/10.1175/MWR3307.1.

Whitaker, J. S., and T. M. Hamill, 2002: Ensemble data assimilation without perturbed observations. *Mon. Wea. Rev.*, **130**, 1913–1924, https://doi.org/10.1175/1520-0493(2002)130<1913:EDAWPO>2.0.CO;2.

Xiao, Q. N., Y. H. Kuo, J. Z. Sun, W. C. Lee, E. Lim, Y. R. Guo, and D. M. Barker, 2005: Assimilation of Doppler radar observations with a regional 3DVAR system: Impact of Doppler velocities on forecasts of a heavy rainfall case. *J. Appl. Meteor.*, **44**, 768–788, https://doi.org/10.1175/JAM2248.1.

Xue, M., and W. J. Martin, 2006: A high-resolution modeling study of the 24 May 2002 dryline case during IHOP. Part I: Numerical simulation and general evolution of the dryline and convection. *Mon. Wea. Rev.*, **134**, 149–171, https://doi.org/10.1175/MWR3071.1.

——, K. K. Droegemeier, and V. Wong, 2000: The Advanced Regional Prediction System (ARPS)—A multi-scale nonhydrostatic atmospheric simulation and prediction model. Part I: Model dynamics and verification. *Meteor. Atmos. Phys.*, **75**, 161–193, https://doi.org/10.1007/s007030070003.

——, and Coauthors, 2001: The Advanced Regional Prediction System (ARPS)—A multi-scale nonhydrostatic atmospheric simulation and prediction tool. Part II: Model physics and applications. *Meteor. Atmos. Phys.*, **76**, 143–165, https://doi.org/10.1007/s007030170027.

——, D. H. Wang, J. D. Gao, K. Brewster, and K. K. Droegemeier, 2003: The Advanced Regional Prediction System (ARPS), storm-scale numerical weather prediction and data assimilation. *Meteor. Atmos. Phys.*, **82**, 139–170, https://doi.org/10.1007/s00703-001-0595-6.

——, M. J. Tong, and K. K. Droegemeier, 2006: An OSSE framework based on the ensemble square root Kalman filter for evaluating the impact of data from radar networks on thunderstorm analysis and forecasting. *J. Atmos. Oceanic Technol.*, **23**, 46–66, https://doi.org/10.1175/JTECH1835.1.

Yussouf, N., J. D. Gao, D. J. Stensrud, and G. Q. Ge, 2013: The impact of mesoscale environmental uncertainty on the prediction of a tornadic supercell storm using ensemble data assimilation approach. *Adv. Meteor.*, **2013**, 731647, https://doi.org/10.1155/2013/731647

Zhang, F. Q., M. Zhang, and J. Poterjoy, 2013: E3DVar: Coupling an ensemble Kalman filter with three-dimensional variational data assimilation in a limited-area weather prediction model and comparison to E4DVar. *Mon. Wea. Rev.*, **141**, 900–917, https://doi.org/10.1175/MWR-D-12-00075.1.

Zhang, M., F. Q. Zhang, X. Y. Huang, and X. Zhang, 2011: Intercomparison of an ensemble Kalman filter with three- and four-dimensional variational data assimilation methods in a limited-area model over the month of June 2003. *Mon. Wea. Rev.*, **139**, 566–572, https://doi.org/10.1175/2010MWR3610.1.

Zhu, K. F., Y. Pan, M. Xue, X. Wang, J. S. Whitaker, S. G. Benjamin, S. S. Weygandt, and M. Hu, 2013: A regional GSI-based ensemble Kalman filter data assimilation system for the rapid refresh configuration: Testing at reduced resolution. *Mon. Wea. Rev.*, **141**, 4118–4139, https://doi.org/10.1175/MWR-D-13-00039.1.